Cell Reports

Article

Neuropeptide CRH prevents premature differentiation of OPCs following CNS injury and in early postnatal development

Graphical abstract

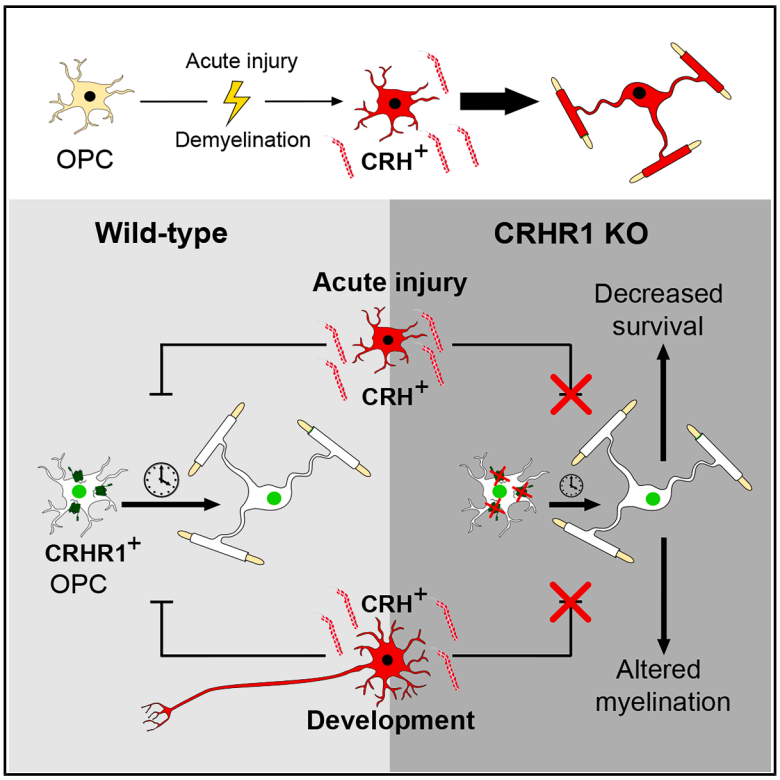

Highlights

- A subset of OPCs transiently produces the neuropeptide CRH in response to injury
- CRHR1$^+$ OPCs are present in the murine brain under injury and non-injury conditions
- CRH$^+$ and CRHR1$^+$ OPCs exhibit distinct differentiation capacities
- Modulation of the CRH/CRHR1 system affects OPC differentiation and myelin structure

Authors

Clemens Ries, Tibor Stark, Benoit Boulat, ..., Wiebke Möbius, Leda Dimou, Jan M. Deussing

Correspondence

clemens.ries@ki.se (C.R.), deussing@psych.mpg.de (J.M.D.)

In brief

Ries et al. identify a population of OPCs distinguished by injury-induced production of CRH. Using specific reporter and knockout mice, they reveal its impact on the oligodendrogenic potential of distinct CRHR1-expressing OPCs. Disrupting CRH/CRHR1 signaling alters developmental oligodendrogenesis and adult myelin structure, uncovering a neuropeptide-based regulatory axis in oligodendrocyte biology.

Ries et al., 2025, Cell Reports *44*, 116474
November 25, 2025
https://doi.org/10.1016/j.celrep.2025.116474

CellPress

Cell Reports

CellPress
OPEN ACCESS

Article

Neuropeptide CRH prevents premature differentiation of OPCs following CNS injury and in early postnatal development

Clemens Ries,[1,12,*] Tibor Stark,[2] Benoit Boulat,[2] Torben Ruhwedel,[3] Jan Philipp Delling,[4] Antonio Miralles Infante,[5] Julia T. von Poblotzki,[1,6] Alessandro Ulivi,[7,8] Iven-Alex von Mücke-Heim,[1] Simon Chang,[1,9,13] Kenji Sakimura,[10] Keiichi Itoi,[11] Dennis B. Nestvogel,[4] Alessio Attardo,[7] Michael Czisch,[2] Klaus-Armin Nave,[3] Wiebke Möbius,[3] Leda Dimou,[5] and Jan M. Deussing[1,14,*]

[1]Max Planck Institute of Psychiatry, Molecular Neurogenetics, Munich, Germany
[2]Max Planck Institute of Psychiatry, Neuroimaging Core Unit, Munich, Germany
[3]Max Planck Institute of Multidisciplinary Sciences, Göttingen, Germany
[4]Max Planck Institute of Psychiatry, Neural Dynamics and Behavior, Munich, Germany
[5]Molecular and Translational Neuroscience, Department of Neurology, Ulm University, Ulm, Germany
[6]Leibnitz Institute for Immunotherapy, Epigenetic Immunooncology, Regensburg, Germany
[7]Leibniz Institute for Neurobiology, Department of Cellular Neuroscience, Magdeburg, Germany
[8]Institute of Genetics, Molecular and Cellular Biology, Strasbourg, France
[9]Translational Genetics, Helmholtz Pioneer Campus, Helmholtz Centre Munich, Munich, Germany
[10]Department of Animal Model Development, Brain Research Institute, Niigata University, Niigata 951-8585, Japan
[11]Super-Network Brain Physiology, Graduate School of Life Sciences, Tohoku University, Sendai 980-8577, Japan
[12]Present address: Karolinska Institutet, Department of Medical Biochemistry and Biophysics, Stockholm, Sweden
[13]Present address: Cellular Neurobiology, Faculty of Biology and Preclinical Medicine, University of Regensburg, Regensburg, Germany
[14]Lead contact
*Correspondence: clemens.ries@ki.se (C.R.), deussing@psych.mpg.de (J.M.D.)
https://doi.org/10.1016/j.celrep.2025.116474

SUMMARY

The role of neuropeptides and their receptors in oligodendrocyte (OL) progenitor cells (OPCs) has been largely overlooked so far. Here, we describe a new subpopulation of corticotropin-releasing hormone (CRH)-expressing OPCs. Brain injury rapidly induces transient CRH expression in OPCs that aggregate around injury sites and exhibit an elevated capacity to differentiate into myelinating OLs. As target cells, we identified CRH receptor type 1 (CRHR1)-expressing OPCs, which show a decreased differentiation velocity. CRH/CRHR1 system inactivation increases the speed of OL generation but compromises their long-term survival after acute injury. Under non-injury conditions, CRH/CRHR1 system deficiency leads to increased early postnatal oligodendrogenesis and alterations in adult myelination. Altogether, we show that OPC-derived CRH not only actively influences the injury environment through interaction with CRHR1-expressing OPCs but also identify the G-protein coupled receptor CRHR1 as a critical modulator of oligodendrogenesis during early postnatal development with lasting effects on adult myelination.

INTRODUCTION

Oligodendrocyte (OL) progenitor cells (OPCs) are the main source of myelinating OLs and have been widely accepted as the fourth major glial cell type of the central nervous system (CNS).[1–3] Upon acute CNS injury, OPCs proliferate, migrate toward the injury site, and differentiate into OLs.[4–8] In regeneration, as well as in development and adulthood, oligodendrogenesis is an inefficient process characterized by an overproduction of premyelinating OLs, of which only a fraction reaches the mature stage.[9–11] While the exact mechanisms of differentiation initiation and myelination are still not fully understood, they have already been shown to be influenced by many different factors, including neuronal activity and G-protein coupled receptor (GPCR) signaling, e.g., by the kappa opioid receptor and its neuropeptide ligand dynorphin.[10,12–14]

Neuropeptides, such as dynorphin, constitute a diverse and heterogeneous group of signaling molecules that target a wide range of structures and biological functions. Stored in large, dense-core vesicles, they signal via a mode known as volume transmission, which distinguishes these neuromodulators from classical neurotransmitters. Accordingly, locally released neuropeptides can have biological effects in a micrometer range.[15,16] Neuropeptides are typically released in large quantities and exert their biological functions through binding and signaling via GPCRs present on target cells. One of the best-studied neuropeptides is the corticotropin-releasing hormone (CRH), which is expressed in neurons throughout the brain. Together with its high-affinity receptor,

CRH receptor type 1 (CRHR1), CRH orchestrates the neuroendocrine, autonomic and behavioral stress response.[17,18] While the CRH/CRHR1 system has anecdotally been reported to affect the brain's reaction to physical damage, its role in injury-connected regenerative processes is unknown.[19,20]

In this study, we identify a CRH/CRHR1 system in OPCs that is activated in response to injury. We show that a subpopulation of OPCs rapidly induces CRH expression following acute injury, which acts through CRHR1 on a separate OPC population to modulate OL generation. Furthermore, we demonstrate that the CRH/CRHR1 system influences the dynamics of oligodendrogenesis not only following injury but also under non-injury conditions during early postnatal and adult stages.

RESULTS

De novo expression of CRH in a subpopulation of OPCs in response to acute brain injury

To study the distribution and connectivity of CRH-expressing neurons in the murine brain, stereotaxic injections of fluorescent retro-beads were performed in the ventral tegmental area (VTA) of *CRH-Cre::Ai9* reporter mice, in which CRH expression is reported via tdTomato (Figures 1A and 1B; Table S1). Analyzing injected brains, we consistently observed an aggregation of tdTomato$^+$ cells with non-neuronal morphology in close proximity to the injection site (Figure 1C). Since the involvement of CRH in the reaction to brain damage was largely unknown, this intriguing observation demanded further investigation. First, we assessed whether *de novo* CRH expression upon acute injury represents a global phenomenon by inflicting injuries in *CRH-Cre::Ai9* mice in the (1) prefrontal cortex (CX), (2) striatum, and (3) midbrain (MB). In all regions, the appearance of tdTomato$^+$ cells was observed 3 days post injury (dpi; Figure 1D). To specify the identity of the newly appearing tdTomato$^+$ cells, immunostainings for different glial (GFAP, Iba1, and NG2) and neuronal (NeuN) markers were performed (Figures 1E and S1A–S1C). Non-neuronal tdTomato$^+$ cells around the injury site only showed co-localization with the OPC marker NG2, specifying these cells as OPCs (Figure 1E). Using the intersectional reporter mouse line *CRH-FlpO::NG2-CreERT2::Ai65*, in which co-expression of CRH and NG2 triggers the expression of tdTomato in a FlpO- and Cre-dependent manner, CRH expression in OPCs was confirmed (Figures 1F and 1G; Table S1). To have a direct measure of CRH expression upon acute injury, we used combined immunostaining against CRH and the OPC-specific marker PDGFRα, showing clear co-localization in several cells surrounding the injury site (Figures 1H and 1H′). Characteristic for a neuropeptide, CRH was localized in vesicular structures throughout the PDGFRα$^+$ cells. In summary, we demonstrate that OPCs express the neuropeptide CRH as a reaction to acute injury.

CRH-expressing OL lineage cells exhibit a strong proliferative response

To better characterize the injury model, we analyzed the injury site over time, focusing on neuronal population recovery (NeuN; Figures S1D and S1E), cell density in the injury core (Figure S1F), and the appearance of astrocytes (GFAP; Figure S1G) and microglia (Iba1; Figure S1H). While reactive astrocytes and microglia were both present early following injury (Figures S1G and S1H), only reactive astrocytes persisted around the injury site at later time points (data not shown). Although the injury site decreased in diameter over time, it did not fully recover—neither in terms of the neuronal population nor with respect to overall cell density within the core (Figures S1D–S1F). To interrogate the population dynamics of CRH-expressing OL lineage cells (OLCs), we first focused on their proliferative capacity and analyzed changes in their cell number after injury. To analyze short- and long-term changes, *CRH-Cre::Ai9* mice were subjected to stab wound injury in the MB and sacrificed at 1, 2, 3, 7, 14, 23, 69, or 128 dpi (Figure 2A). tdTomato$^+$/Olig2$^+$ cells were quantified in a 300-μm radius around the wound center with 50–100-μm medio-lateral resolution (Figures 2B and 2C; Methods S1A–S1C). Quantification in the whole area revealed a considerable increase of tdTomato$^+$/Olig2$^+$ cells between 2 (14 ± 8.13/mm^2) and 7 dpi (168 ± 27.85/mm^2), followed by a significant decrease until 128 dpi (55 ± 6.56 cells/mm^2; Figure 2C). Also, within the first 50 μm around the wound center, dynamics were comparable with a considerably higher density (614 ± 87.62 cells/mm^2; Figure S2A). The medio-lateral distribution of CRH-expressing OLCs over time shows their initial appearance within the entire area of analysis (0–300-μm distance), with a progressive inward movement over time (Figure 2C, heatmap). Because of the well-described proliferative reaction of OPCs following insult,[6] we investigated whether cell division following CRH expression contributed to the increase in total cell number. Indeed, tdTomato$^+$/Olig2$^+$ cells showed not only *de novo* expression of CRH but also co-expression of the proliferation marker Ki67 (Figure 2D). Quantification revealed that, while at 2 dpi, the vast majority of Olig2$^+$/tdTomato$^+$ cells were Ki67$^+$ (98 ± 1.75%), the proportion of co-expressing cells dropped significantly until 7 dpi (18% ± 2.31%; Figures 2E and S2B).

CRH-expressing OPCs mature into myelinating OLs

One function of OPCs in the context of brain injury is regeneration of the OL population.[5] Therefore, we investigated the fate of CRH-expressing cells in more detail by evaluating their differentiation capacity using NG2/Olig2 and CC1/Olig2 double staining. At the time of their first appearance between 2 and 3 dpi, all (100% ± 0%) of tdTomato$^+$/Olig2$^+$ cells were also NG2$^+$ (Figures 2F and S2C). No co-localization with the OL marker CC1 was found. Subsequently, the proportion of NG2$^+$ cells of the tdTomato$^+$/Olig2$^+$ population steadily decreased, reaching a minimum at 128 dpi (7.67% ± 4.10%), while the percentage of CC1$^+$ cells among tdTomato$^+$/Olig2$^+$ cells continuously increased until 128 dpi (76.33% ± 3.67%; Figures 2F, 2G, and S2D). CRH$^+$ OLCs possessed OL-like morphologies and were present in the MB as well as in the white matter (WM; Figure 2H). The myelinating character of these cells was further confirmed by co-localization with the myelin proteins CNPase and MBP within their processes at 4 months post injury (Figure 2I). These results indicate that CRH-expressing OPCs predominantly mature into myelinating OLs after acute injury and are highly stable once integrated. To further substantiate these findings on a single-cell level, we used *CRH-Cre::Ai9* and *CRH-FlpO::NG2-CreERT2::Ai65* mice for repeated *in vivo* two-photon imaging. For cortical imaging, a cranial window

CellPress
OPEN ACCESS

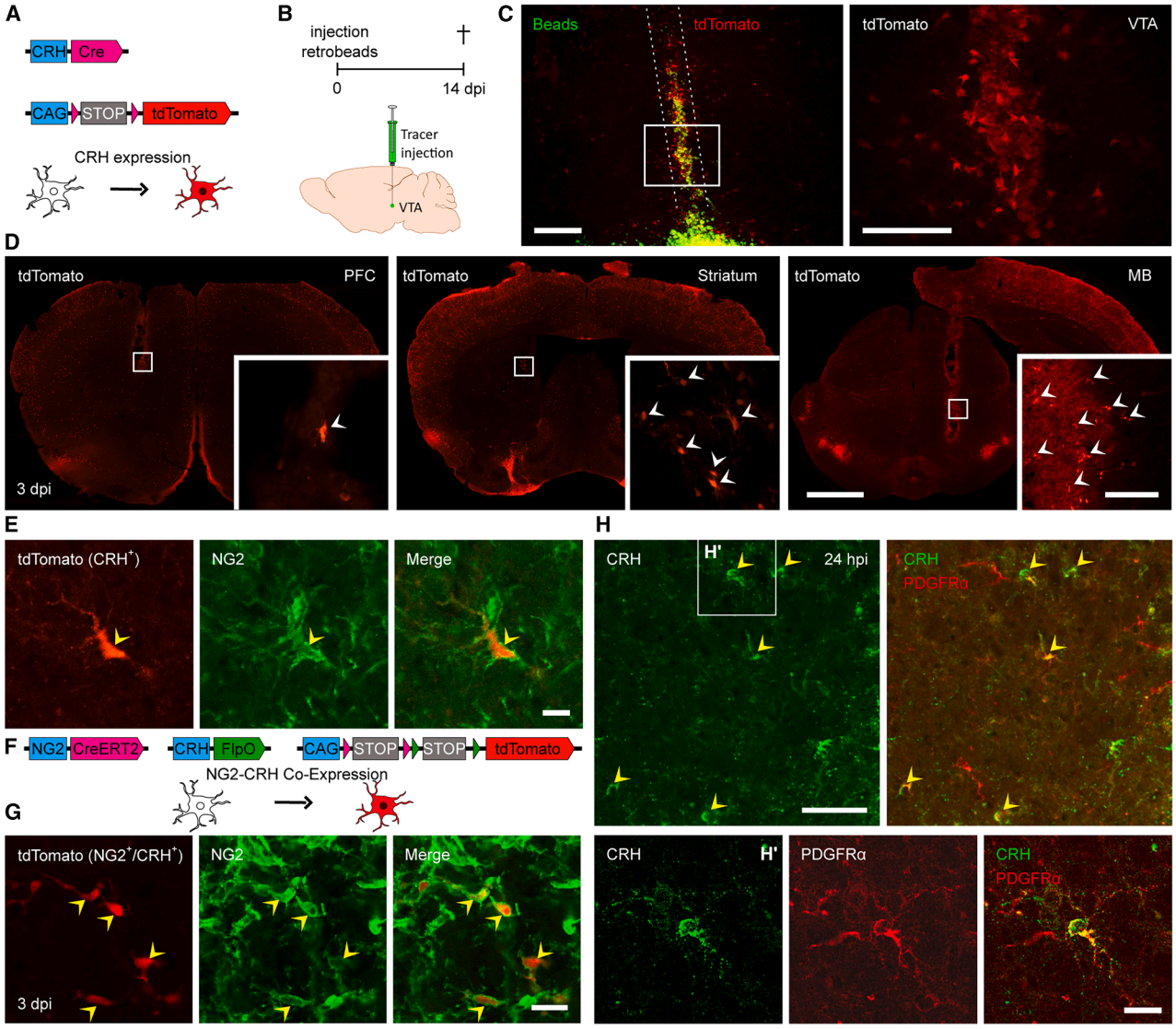

Figure 1. Identification of CRH-expressing OPC subpopulation

(A) The *CRH-Cre::Ai9* model.

(B) Experimental setup and injection site.

(C) Injection site of fluorescent beads and needle tract (framed by white dotted lines). Scale bars, 100 μm.

(D) Aggregation of CRH-expressing (tdTomato$^+$) cells around injury sites in the PFC, striatum, and MB in *CRH-Cre::Ai9* mice. Scale bars, 1000 μm (overview) and 50 μm (close up).

(E) Immunostaining for NG2 at the injury site in *CRH-Cre::Ai9* mice. Scale bar, 10 μm.

(F) Intersectional reporter mouse line *CRH-FlpO::NG2-CreERT2::Ai65*.

(G) Confocal images of NG2/CRH co-expressing (tdTomato$^+$) cells at injury site at 3 dpi stained for NG2. Scale bar, 20 μm.

(H) Confocal image of combined CRH/PDGFRα staining at 24 hpi. Scale bar, 50 μm.

(H′) Magnification of CRH/PDGFRα-co-expressing cell. Scale bar, 20 μm.

For all images, white arrowheads indicate cells or structures. Yellow arrowheads indicate co-localization of indicated markers.

in combination with an acute stab wound injury was used in *CRH-Cre::Ai9* mice (Figures 3A, 3B, and S3A). To image WM processes, a cannula was implanted into the CX, resembling an injury itself (Figure 3A). Using these methods, single cells were identified and followed over several weeks, confirming proliferation (Figure S3B), movement toward the injury site (Figure S3C), and the subsequent maturation, as can be inferred from the morphological changes leading to the characteristic appearance of a myelinating OL (Figure 3C). On top of that, long-term imaging in the WM of *CRH-FlpO::NG2-CreERT2::Ai65* mice (cannula implantation) revealed that mature OLs persisted over the entire imaging period (Figures S3D–S3G″ and S3H–S3K). These findings collectively identify CRH-expressing OPCs as a highly proliferative subpopulation of OPCs, highlighting their strong propensity for

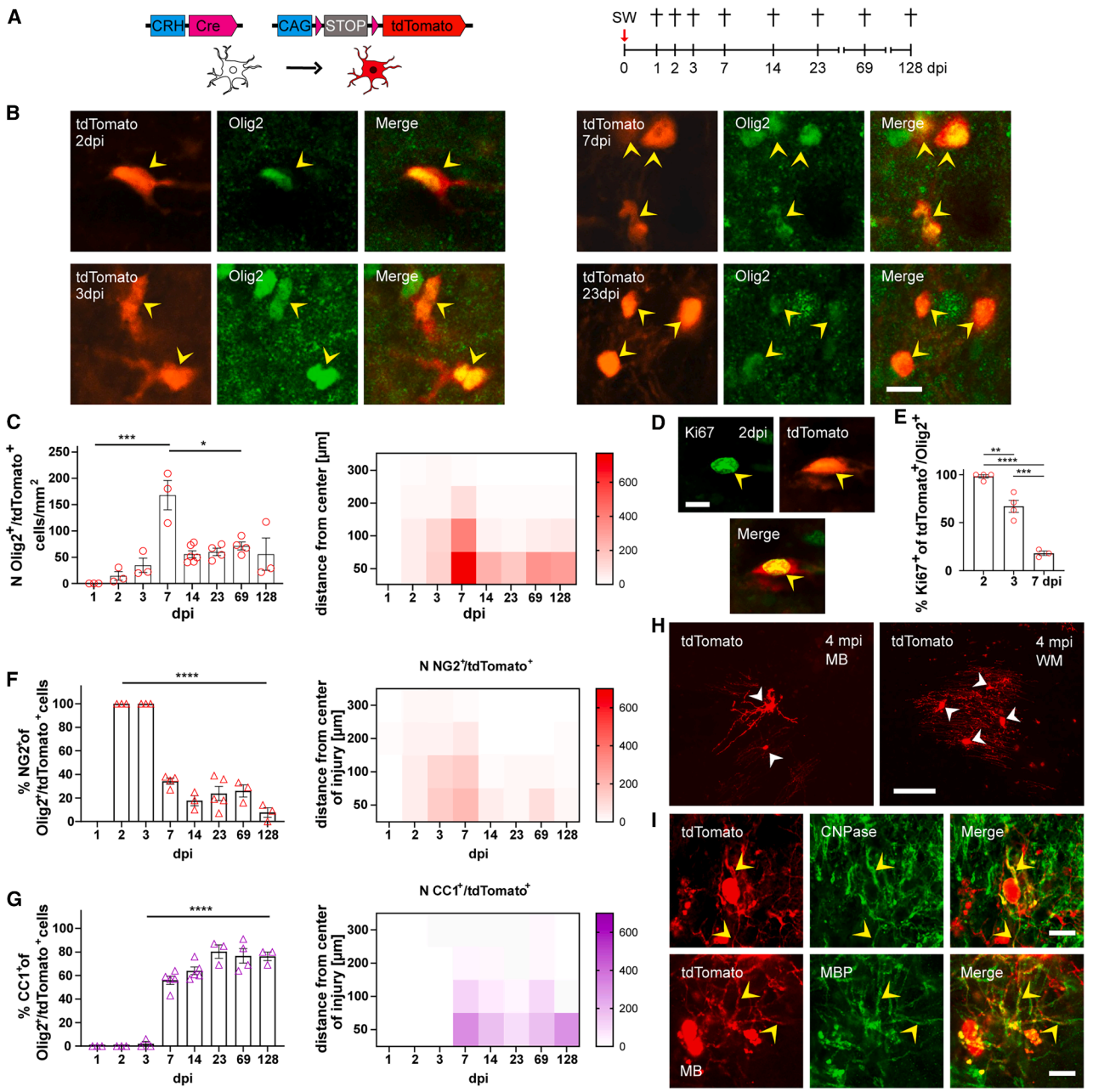

Figure 2. CRH$^+$ OLCs proliferate and generate myelinating OLs following injury

(A) The *CRH-Cre::Ai9* model and experimental setup.

(B) Representative confocal images of Olig2 staining at different time points. Scale bar, 10 µm.

(C) Quantification of Olig2$^+$/tdTomato$^+$ cells at ±300 µm around the injury site, and heatmap showing spatiotemporal appearance of Olig2$^+$/tdTomato$^+$ cells, n_{TP} = 3–6 mice.

(D) Confocal image of Ki67 staining at 2 dpi. Scale bar, 10 µm.

(E) Quantification of Ki67$^+$/tdTomato$^+$/Olig2$^+$ cells of all tdTomato$^+$/Olig2$^+$ cells at 2–7 dpi. n_{TP} = 3–4 mice.

(F) Left, percentage of NG2$^+$/Olig2$^+$/tdTomato$^+$ cells of all Olig2$^+$/tdTomato$^+$ cells. Right, number of NG2$^+$/tdTomato$^+$ cells in spatiotemporal resolution. n_{TP} = 3–6 mice.

(G) Left, percentage of CC1$^+$/Olig2$^+$/tdTomato$^+$ cells of all Olig2$^+$/tdTomato$^+$ cells. Right, number of CC1$^+$/tdTomato$^+$ cells in spatiotemporal resolution. n_{TP} = 3–6 mice.

(H) Morphologies of tdTomato$^+$ cells at 4 mpi in the MB (left) and WM (right). Scale bar, 50 µm.

(I) Confocal images of anti-CNPase and anti-MBP staining. Scale bar, 10 µm.

For all images, white arrowheads indicate cells or structures. Yellow arrowheads indicate co-localization of indicated markers. All data points represent individual animals. All *p* values are from one-way ANOVA test, $^*p < 0.05$ and $^{****}p < 0.0001$; data are shown as mean ± SEM.

CellPress
OPEN ACCESS

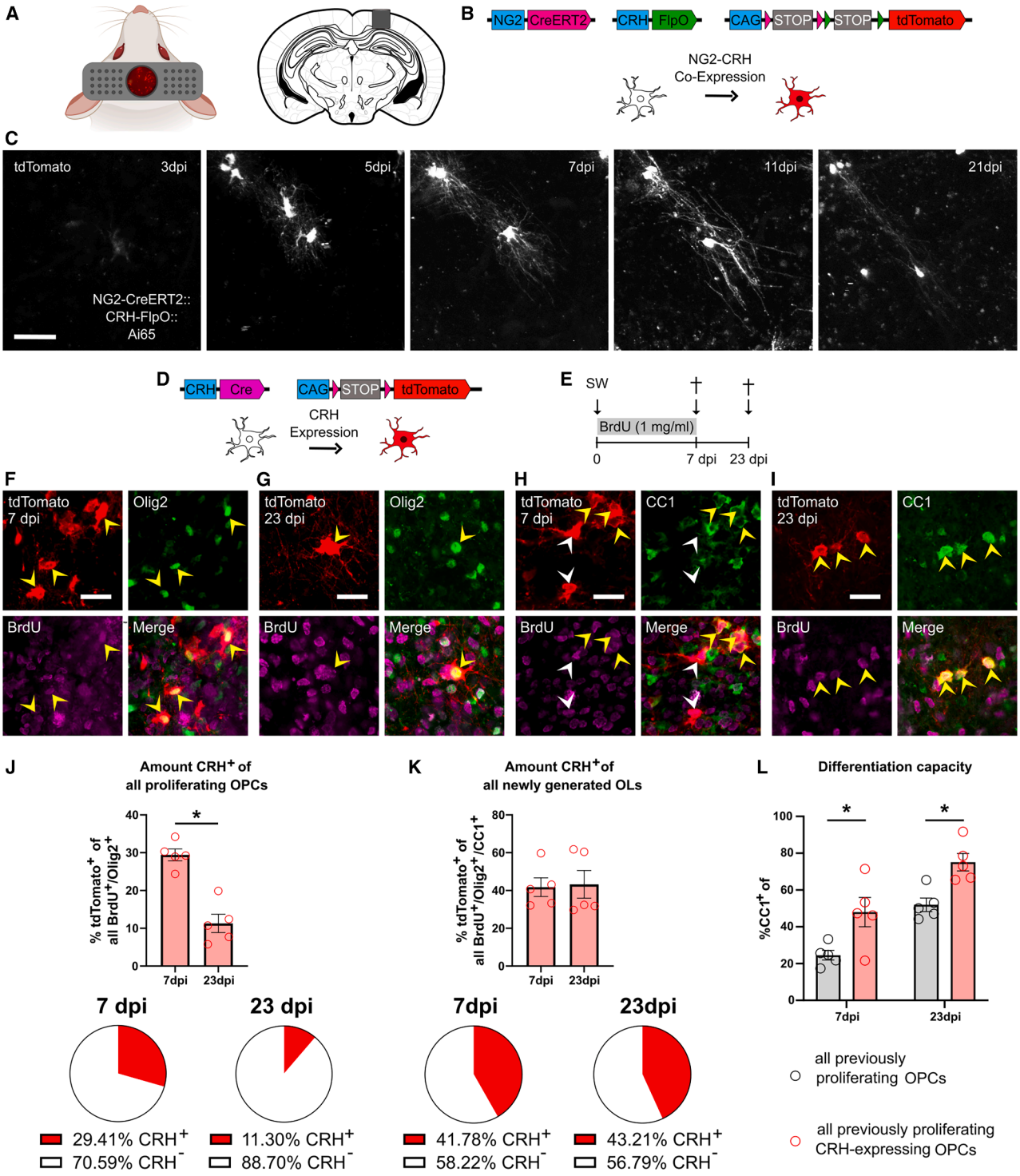

Figure 3. CRH⁺ OPCs show elevated differentiation capacity compared to CRH⁻ OPCs

(A) Graphical illustration of the field of view during *in vivo* 2-photon imaging (left) and the position of the imaging cannula (right).

(B) Intersectional reporter mouse line *CRH-FlpO::NG2-CreERT2::Ai65.*

(C) Representative 2-photon images of tdTomato⁺ OPCs in one ROI after implantation of hippocampal cannula maturing into OLs. Scale bar, 50 μm.

(D) *CRH Cre::Ai9* mouse line.

(E) Experimental setup of label-retaining experiment.

(F and G) Confocal images of tdTomato, Olig2, and BrdU colocalization at 7 (F) and 23 dpi (G). Scale bar, 20 μm.

(legend continued on next page)

oligodendrogenesis and their long-term stability following successful integration.

CRH-expressing OPCs contribute substantially to OL generation following injury

To assess the size and dynamics of the CRH-expressing OLC subpopulation in relation to the entire OLC population, we utilized the robust proliferative response of OPCs following injury. We conducted a label-retaining experiment in *CRH-Cre::Ai9* mice post-insult using the intercalating substance 5-bromo-2′-deoxyuridine (BrdU), which labels all proliferating cells (Figures 3D and 3E). BrdU$^+$ OLCs were identified at 7 and 23 dpi (Figures 3F–3I). The quantification of all tdTomato$^+$/Olig2$^+$/BrdU$^+$ cells and the amount of BrdU$^+$ cells in the total tdTomato$^+$/Olig2$^+$ cell population around the injury site revealed a decrease between 7 (174.0 ± 14.65 cells/mm^2) and 23 dpi (80.11 ± 15.52 cells/mm^2) and confirmed the previously found (Figures 2D and 2E) high percentage (7 dpi: 94.23% ± 1.83%; 23 dpi: 93.50% ± 3.24%) of proliferating cells in the CRH-expressing OPC population (Figures S4A and S4B). The fact that the percentage of BrdU$^+$ cells in the total previously proliferating OPC population (Olig2$^+$/BrdU$^+$) was 29.41% ± 1.57% at 7 dpi (Figure 3J) shows the significant contribution of the CRH-expressing population to all proliferating OPCs.

Furthermore, when examining the proportion of CRH-expressing OLCs in the newly generated OL population (BrdU$^+$/CC1$^+$), we found that they consistently accounted for approximately 40% of newly generated OLs at both 7 dpi (41.78% ± 4.94%) and 23 dpi (43.21% ± 7.33%; Figure 3K). To determine if this strong and persistent contribution was caused by a higher differentiation rate, we evaluated the percentage of CC1$^+$ cells within the population of CRH-expressing and all formerly proliferating OLCs. CRH-expressing OLCs demonstrated a significantly increased likelihood of being CC1$^+$ at both 7 (all: 24.57% ± 2.62%; CRH$^+$: 48.00% ± 8.00%) and 23 dpi (all: 51.95% ± 3.68%; CRH$^+$: 75.10% ± 4.76%) (Figure 3L).

In summary, these results indicate that CRH-expressing OLCs constitute 30% of all proliferating OLCs at 7 dpi and, due to their higher differentiation capacity, contribute approximately 40% to the population of newly generated OLs following injury.

Induction of CRH expression in OPCs is an early response to brain injury

After defining the key properties of CRH-expressing OPCs with regards to proliferation and maturation, we focused on the injury-induced expression of the neuropeptide CRH itself. To this end, we took advantage of the *CRH-Venus* mouse line[21] in which Venus was inserted in the *Crh* locus, which facilitates direct monitoring of CRH expression via the reporter (Figure 4A; Table S1). This enabled us to visualize the distribution of CRH$^+$ cells and provided a proxy to assess CRH expression kinetics as these are directly correlated with the Venus expression driven by the endogenous *Crh* promoter. Following injury, Venus$^+$/NG2$^+$ cells were identified around the injury site (Figure 4A). Furthermore, CRH was identified in Venus$^+$ cells, validating Venus as a proxy for CRH expression (Figures 4B and 4B′). To assess CRH expression kinetics, Venus$^+$/Olig2$^+$ OPCs (at early time points $N_{CRH^+Olig2^+} = N_{CRH^+NG2^+}$; Figure 2F) were quantified around the injury site at different time points between 12 and 168 h post injury (hpi; Figure 4C). The first Venus$^+$ OPCs were detected as early as 12 hpi, indicating that CRH is expressed as an immediate reaction to the injury (Figure 4C). Between 12 (12 ± 2.08 cells) and 48 hpi (80.33 ± 12.39 cells), the number of Venus-expressing OPCs increased. After 96 (6.67 ± 0.88 cells) and 168 hpi (4.67 ± 1.20 cells), only few cells were traceable, suggesting that Venus and, thus, CRH expression predominantly occur within the first 3 to 4 dpi. Notably, at 12 and 24 hpi, all cells were present as individual single cells, whereas at 36 (46.25% ± 0.94%) and 60 hpi (76.74% ± 3.22%), a high proportion of cells were part of a cluster, likely emerging from proliferation (Figure S4C). Indeed, immunostaining revealed that a large proportion of Venus$^+$ cells were also Ki67$^+$ but only starting from 36 hpi (39.73% ± 2.83%) onwards (Figure S4D). These results, in combination with the observation that the vast majority of Olig2$^+$/tdTomato$^+$ cells was Ki67$^+$ at 2 dpi (98% ± 1.75%) in the *CRH-Cre::Ai9* model (Figure 2E), indicate that in the sequence of reactions to injury, CRH expression precedes proliferation.

CRHR1-expressing OPCs resemble a distinct population and are potential targets of OPC-derived CRH

The canonical high-affinity receptor of CRH is CRHR1. To identify potential target cells of CRH release, we investigated the presence of CRHR1-expressing glial cells in the vicinity of the wound. Therefore, we used the *CRHR1-Cre::Tau-LSL-FlpO::Ai9* mouse model, in which tdTomato expression is activated in all CRHR1$^+$ cells but selectively deleted from CRHR1$^+$ neurons (Figure 4D; Table S1). When analyzing stab wounds at 3 dpi, we found CRHR1-expressing cells aggregating around the injury site that were identified as OPCs by NG2 staining (Figure 4E) and very few as astrocytes by GFAP and S100β staining (Figures S4E–S4I). The CRHR1-expressing OPCs were also shown to differentiate into myelinating OLs at 6 wpi by MBP staining following tissue expansion[22,23] (Figure 4F). To our surprise, CRHR1$^+$/NG2$^+$ cells were also present on the non-injured contralateral site and also throughout the brain under non-injury

(H and I) Confocal images of tdTomato, CC1, and BrdU colocalization at 7 (H) and 23 dpi (I). Scale bar, 20 μm.
(J) Amount of CRH$^+$ (tdTomato$^+$) cells of all BrdU$^+$/Olig2$^+$ cells, and pie charts illustrating proportions of CRH$^+$ and CRH$^-$ cells in whole population of previously proliferating OLCs over time. $n_{TP} = 5$ mice.
(K) Amount of CRH$^+$ (tdTomato$^+$) cells in BrdU$^+$/CC1$^+$ newly generated OLs, and pie charts illustrating proportions of CRH$^+$ and CRH$^-$ cells in whole population of newly generated OLs. $n_{TP} = 5$ mice.
(L) Amount of CC1$^+$ cells of CRH-expressing and all previously proliferating OLCs. $n_{TP} = 5$ mice.
For all images, white arrowheads indicate cells or structures. Yellow arrowheads indicate co-localization of indicated markers. All data points represent individual animals. The *p* values are from Welch-corrected two-tailed t test (J–K) and two-way ANOVAs with Sidak's post hoc test (L), $^*p < 0.05$, $^{****}p < 0.0001$, data are shown as mean ± SEM.

CellPress
OPEN ACCESS

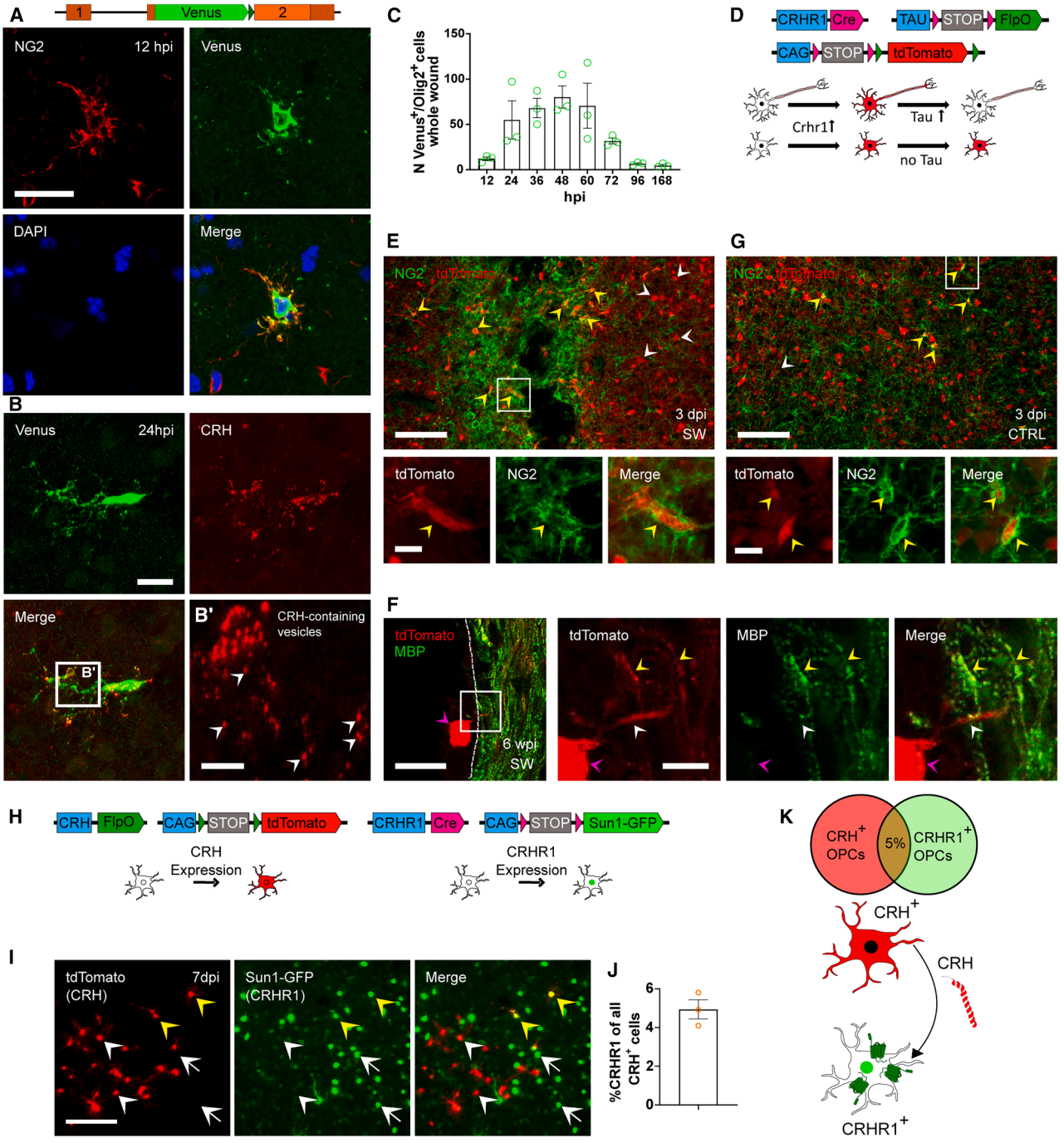

Figure 4. OPC-derived CRH targets distinct CRHR1$^+$ OPC population

(A) The *CRH-Venus* reporter mouse model. Representative confocal images of NG2/GFP co-localization at 12 hpi. Scale bar, 20 μm.

(B) Confocal image of GFP-expressing cell at injury site in *CRH-Venus* mice stained for CRH protein. Scale bars, 20 μm.

(B′) Magnification of CRH staining. Scale bar, 5 μm.

(C) Quantification of GFP$^+$/Olig2$^+$ cells around the injury site between 12 and 168 hpi. n_{TP} = 3 mice.

(D) The *CRHR1-Cre::Tau-LSL-FlpO::Ai9* mouse model.

(E) Confocal image of NG2 staining around the wound identifying cells as CRHR1-expressing OPCs. Scale bars, 100 μm (overviews), 10 μm (insets).

(F) Confocal image of colocalization of MBP$^+$ and tdTomato$^+$ process at injury site at 23 dpi following tissue expansion. Scale bar, 100 μm.

(G) Confocal image of NG2$^+$/tdTomato$^+$ cells at the uninjured contralateral side at 3 dpi identifying cells as CRHR1-expressing OPCs. Scale bars, 100 μm (overviews), 10 μm (insets).

(legend continued on next page)

conditions (Figure 4G). To better understand this potential interaction between OPC-derived CRH and CRHR1 on OPCs, we tested whether CRHR1 expression persisted in adulthood. Due to the lack of reliable CRHR1-specific antibodies, we had to choose other approaches for detection of CRHR1 expression.[24] Thus, we validated the expression of CRHR1 in OLCs by (1) direct visualization of CRHR1 expression in *CRHR1*$^{\Delta EGFP}$ mice and (2) AAV-mediated reporting of CRHR1 expression. To assess CRHR1 expression in OPCs under physiological conditions, we took advantage of the *CRHR1*$^{\Delta EGFP}$ mouse line, which is characterized by a knockin of GFP into the *Crhr1* locus, which serves as valid proxy for CRHR1 expression (Figure S4J; Table S1).[24] Co-staining with PDGFRα showed clear co-localization with GFP-expressing cells of the WM, identifying these cells as OPCs (Figures S4K and S4K′). For AAV-mediated reporting, we used an AAV harboring the DIO-GFP system, which was injected in *CRHR1-Cre* mice (Figure S4L). Following Cre-mediated recombination, GFP was activated in all CRHR1-expressing cells. CRHR1$^+$ OLCs were specifically identified by Olig2 colocalization (Figures S4M and S4M′).

The identification of CRHR1-expressing OPCs surrounding the injury site raised the question whether ligand and receptor are cellularly co-expressed or exist in distinct OPC populations. To quantify the overlap, we used the *CRH-FlpO::CRHR1-Cre::Ai65F::Sun1-GFP* mouse line in which CRH expression is reported by tdTomato and CRHR1 expression by GFP fused to the nuclear membrane localization marker SUN1 (Figure 4H; Table S1). TdTomato$^+$ (CRH) and GFP$^+$ (CRHR1) cells were identified around the injury site but only showed an overlap of 4.9% ± 0.49% (Figures 4I and 4J), thereby clearly separating the CRH- and CRHR1-expressing populations of OPCs (Figure 4K). Taken together, these observations evidently demonstrate that CRHR1 is expressed in a distinct OPC population, qualifying it as a potential target of CRH released following injury.

CRHR1$^+$ OPCs show a delayed differentiation following injury

To investigate the differences between CRHR1- and CRH-expressing OPCs following injury, we conducted a label-retaining experiment using *CRHR1-Cre::Sun1-GFP* animals (Figures 5A and 5B; Table S1). These animals were subjected to injury, treated with BrdU for 3 or 7 days, and sacrificed at 3, 7, and 23 dpi. GFP$^+$/BrdU$^+$/Olig2$^+$ and GFP$^+$/BrdU$^+$/CC1$^+$ cells were identified at all time points (Figures 5C–5F).

First, we assessed the number of previously proliferating CRHR1$^+$ OLCs (GFP$^+$/Olig2$^+$/BrdU$^+$), noting a significant increase in cell numbers from 3 (21.25 ± 12.53/mm^2) to 7 dpi (100.4 ± 7.80/mm^2), followed by a non-significant decrease toward 23 dpi (72.31 ± 6.70/mm^2; Figure 5G).

We then analyzed the proportion of CRHR1-expressing OLCs (GFP$^+$/BrdU$^+$/Olig2$^+$) within the population of all previously proliferating OLCs (BrdU$^+$/Olig2$^+$). The proportion increased slightly from 11.57% ± 5.34% at 3 dpi to 17.70% ± 3.62% at 7 dpi, subsequently remaining steady until 23 dpi (16.01% ± 2.09%; Figure 5H), showing that the CRHR1-expressing population of OPCs contributed significantly to the population of proliferating OPCs.

To evaluate the differentiation capacity of CRHR1-expressing OPCs, we compared the percentage of CC1$^+$ cells in the overall BrdU$^+$ and within the CRHR1$^+$ population. Our analysis revealed a significantly lower percentage of CC1$^+$ cells among CRHR1-expressing OLCs at 7 dpi (all: 29.27% ± 3.22%; CRHR1$^+$: 14.18% ± 1.43%), a difference that dissipated by 23 dpi (all: 44.60% ± 6.42%; CRHR1$^+$: 43.25% ± 5.57%; Figure 5I). This temporary disparity in the probability of a cell being CC1$^+$ between the two populations suggests a delay in the differentiation of CRHR1$^+$ OPCs rather than a fundamental difference in their differentiation potential following injury.

Disruption of the CRH/CRHR1 system affects the OPC population around the injury site

After the identification and characterization of CRHR1-expressing OPCs around the injury site as potential targets of OPC-derived CRH, we investigated the functional impact of the inhibition of the CRH/CRHR1 system on OLCs following insult.

To this end, we pursued different loss-of-function (LOF) approaches using (1) a conditional tamoxifen-inducible NG2-specific CRH KO (*CRH*$^{NG2\text{-}cKO}$) and (2) a global constitutive (*CRHR1*$^{\Delta EGFP}$) and a conditional tamoxifen-inducible NG2-specific CRHR1 KO (*CRHR1*$^{NG2\text{-}cKO}$; Table S1). Before assessing the effect of the NG2-specific CRH KO, the recombination efficiency following tamoxifen treatment was assessed and shown to be at 66.3% ± 1.6% (Figures S5A and S5B). Then, we compared the number of OLs, OPCs, and OLCs and the amount of OLs in the whole population of OLCs (Figures 5J–5M). In *CRH*$^{NG2\text{-}cKO}$ mice, no significant difference was identified in OL or OLC numbers, but the number of OPCs around the injury site was significantly reduced in cKO animals at 7 dpi (Figures 5K, 5N, and 5O). This lower number of OPCs was accompanied by significantly increased proportion of OLs of all OLCs in cKO animals at 7 dpi (Figure 5M).

Similar to *CRH*$^{NG2\text{-}cKO}$ mice, the global loss of CRHR1 expression in *CRHR1*$^{\Delta EGFP}$ led to a significant reduction in OPCs (Figures 5Q, 5T, and 5U) and also to a higher proportion of OLs of all OLCs at 7 dpi (Figure 5S), while the total number of OLs and OLCs was unchanged (Figures 5P and 5R). These effects were neither observed in NG2-specific CRHR1 KO animals (Figures S5C–S5F) nor on the non-injured, contralateral side of

(H) The *CRH-FlpO::CRHR1-Cre::Ai65F::Sun1-GFP* reporter mouse model to study the percentage of overlap between the CRH- and CRHR1-expressing populations of OLCs.

(I) Confocal images of injury site in *CRH-FlpO::CRHR1-Cre::Ai65F::Sun1-GFP* mice at 7 dpi. Scale bar, 100 μm. Arrowheads show tdTomato$^+$/Sun1-GFP$^-$ (white) and tdTomato$^+$/Sun1-GFP$^+$ (yellow) cells. Arrows show Sun1-GFP$^+$/tdTomato$^-$ cells.

(J) Quantification of CRHR1$^+$/CRH$^+$ of all CRH$^+$ cells.

(K) Population overlap between CRH- and CRHR1-expressing OPCs and potential directionality of interaction.

For all images, white arrowheads indicate cells or structures. Yellow arrowheads indicate co-localization of indicated markers. Purple arrowhead indicates soma. All data points represent individual animals. The *p* value is from a one-way ANOVA (C), $^*p < 0.05$, $^{****}p < 0.0001$, data are shown as mean ± SEM.

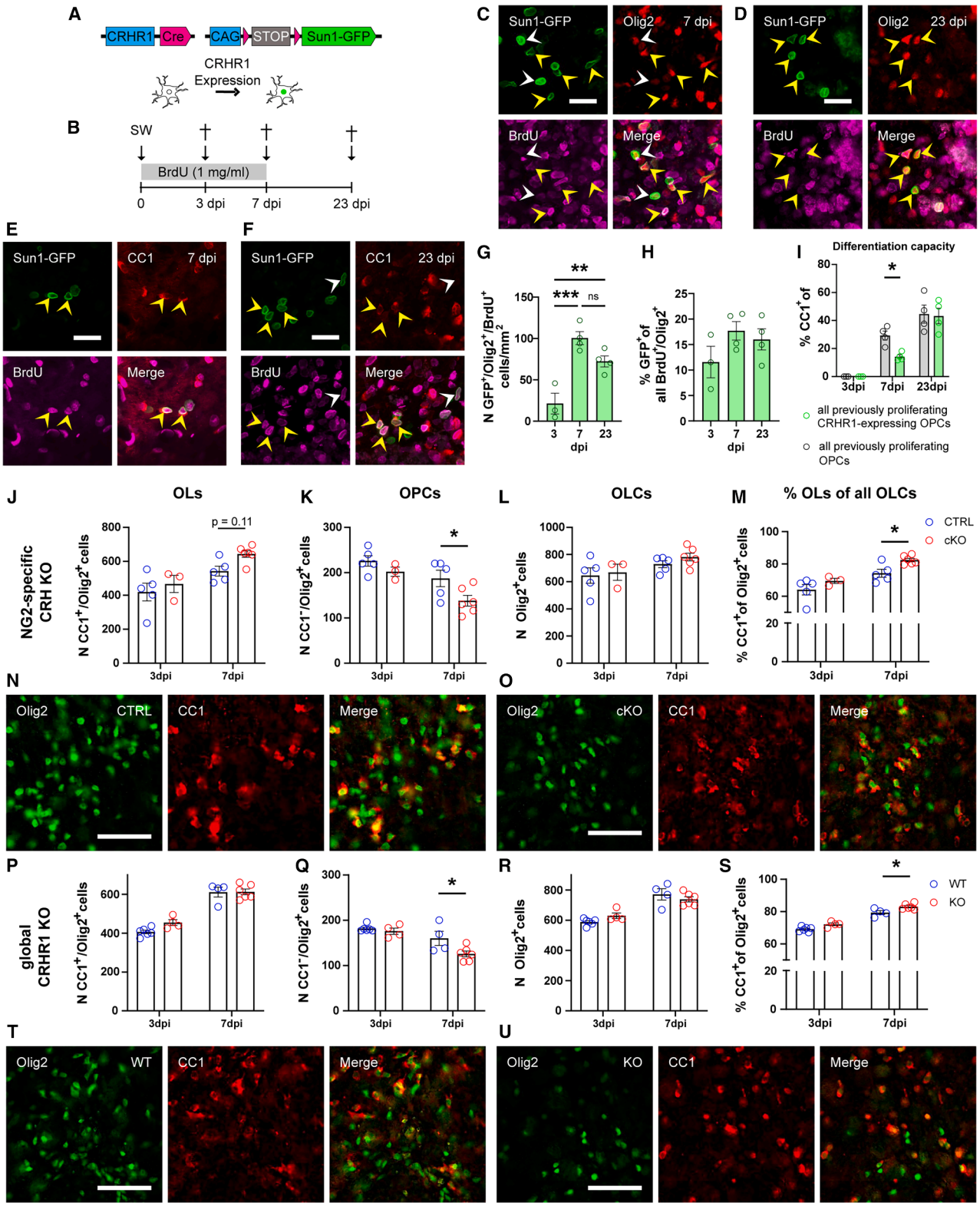

Figure 5. Injury-related population dynamics of CRHR1$^+$ OLCs and effect of CRH/CRHR1 modulation

(A) The *CRHR1-Cre::Sun1-GFP* reporter mouse model.

(B) Experimental timeline of BrdU label-retaining experiment.

(legend continued on next page)

any of the models (Figures S5G–S5L). These results indicated that a decreased CRH/CRHR1 signaling influences the OLC population following injury by altering the dynamics of OPCs.

CRH/CRHR1 system inhibition increases the generation and survival of newly formed OLs in an injury size-dependent manner

The observed reduction of OPCs following CRH/CRHR1 system blockade could have been caused by a reduced proliferation between 3 and 7 dpi or by a faster differentiation rate of OPCs into OLs. To elucidate the cause, we performed a label-retaining experiment using *CRHR1*$^{\Delta EGFP}$ KO mice (Figure 6A). The number of BrdU$^+$, all BrdU$^+$/Olig2$^+$, or BrdU$^+$/Olig2$^+$/CC1$^-$ did not show any significant difference between WT and KO animals, suggesting equal proliferative activation of OPCs and no differences in OPC-specific cell death (Figures 6B, S6A, and S6B). We then quantified the number of BrdU$^+$/Olig2$^+$/CC1$^+$ cells around the injury site and found a significant increase in these newly generated OLs at 7 dpi, which was absent at 6 wpi (Figure 6C). When limiting the analysis to the inner 150 μm of the wound, a significant increase in the total number of OLs (CC1$^+$/Olig2$^+$ cells) was present in KO animals (Figure 6E). The mean difference in the total number of OLs was twice as high as the difference in newly generated ones (BrdU$^+$/Olig2$^+$/CC1$^+$ cells), suggesting that direct differentiation from OPCs without proliferation and concomitant BrdU integration also contributed to these differences. When analyzing the number of newly generated OLs in the first 150 μm, we found a significantly higher number in KO animals compared to WT animals (Figure 6F). Overall, the observed reduction of OPCs in the CRH as well as CRHR1 KO animals was most likely caused by an increased differentiation velocity at early post-injury stages. These differences in OL numbers did not lead to a significant change in MBP staining intensity (Figure S6C) nor other injury-connected parameters in the injury area like revascularization or the number of TNFα$^+$ cells (Figures S6D–S6G).

To assess the influence of the injury size itself on the long-term survival of OLs, we performed another experiment in *CRHR1*$^{\Delta EGFP}$ animals using a 2.5× bigger cannula (diameter 0.5 mm; Figures 6G and 6H). Animals were sacrificed at 6 wpi, and the number of CC1$^+$ OLs was assessed on coronal sections to increase the visible part of the injury. The analysis of the injury site showed a significant decrease in KO compared to WT animals (Figures 6I–6K). Thus, in CRHR1 KO animals, the long-term survival of newly generated OLs is reduced in a threshold-dependent manner, depending on the injury size and the corresponding demand for remyelination. This decrease was likely caused by the CRHR1 KO-induced premature differentiation of OPCs into OLs observed in the previous experiment (Figures 6C–6F).

CRHR1-expressing OLCs increase their numbers in the whole OLC population under non-injury conditions

Because CRH-expressing OPCs are only present in the murine brain following acute injury, but CRHR1-expressing OPCs as well as other sources of CRH, e.g., neurons, are present under naive conditions, we next sought to investigate their functional role under non-injury conditions. To this end, we quantified the number of CRHR1-expressing OLCs at different postnatal time points (1.5, 3, and 5 months) in *CRHR1-Cre::Tau-LSL-FlpO::Ai9* mice (Figure S7A). CRHR1-expressing OLCs were found at all ages (Figures S7B–S7F). Firstly, the total number of CRHR1-expressing OPCs was quantified at all time points in the CX; WM, including the corpus callosum, capsule, and anterior commissure; as well as in the MB. The number of CRHR1-expressing OPCs increased over time, showing a significant gain between 3 and 5 months in the CX (2.61 ± 0.96 to 19.67 ± 3.54 cells/mm^2) and MB (9.78 ± 2.13 to 28.44 ± 8.30 cells/mm^2; Figure S7G). This resulted in a significant increase in the percentage of tdTomato$^+$ OPCs of all OPCs in the CX (1.88% ± 0.35% to 7.07% ± 1.44%) and MB (4.36% ± 0.87% to 10.42% ± 2.64%) but not in the WM (2.09% ± 0.89% to 4.81% ± 0.39%) between 1.5 and 5 months (Figure S7H). In addition, we quantified the total number of tdTomato$^+$/Olig2$^+$ cells, which differed between distinct brain regions and ages. In the CX, the cell numbers were lowest at all time points, while the numbers in WM and MB were comparable at 1.5 and 3 months. Generally, the number of tdTomato$^+$/Olig2$^+$ cells significantly increased toward 5 months of age, which was more pronounced in the WM (100.70 ± 37.35 to 362.78 ± 95.95 cells/mm^2) than in the MB (124.06 ± 19.62 to 217.5 ± 33.17 cells/mm^2; Figure S7I). As the number of OLs increases with age, we investigated whether

(C and D) Confocal images of Sun1-GFP$^+$ (CRHR1$^+$)/Olig2$^+$/BrdU$^+$ cells at 7 (C) and 23 dpi (D).
(E and F) Confocal images of Sun1-GFP$^+$ (CRHR1$^+$)/CC1$^+$/BrdU$^+$ cells at 7 (E) and 23 dpi (F).
(G) Quantification of BrdU$^+$ CRHR1-expressing OLCs at 3, 7, and 23 dpi, n_{TP} = 3–4 mice.
(H) Amount of CRHR1 (GFP)-expressing OPCs of all proliferating (BrdU$^+$/Olig2$^+$) OPCs, n_{TP} = 3–4 mice.
(I) Amount of CC1$^+$ cells of CRHR1-expressing and all previously proliferating OLCs, n_{TP} = 3–4 mice.
(J) Number of CC1$^+$/Olig2$^+$ cells at 3 and 7 dpi in NG2-specific CRH cKO vs. CTRL animals. $n_{TP/GT}$ = 5–6 mice.
(K) Number of CC1$^-$/Olig2$^+$ cells in NG2-specific CRH cKO compared to CTRL animals. $n_{TP/GT}$ = 5–6 mice.
(L) Total number of Olig2$^+$ cells in cKO and CTRL animals, $n_{TP/GT}$ = 5–6 mice.
(M) Percentage of CC1$^+$ of all Olig2$^+$ cells in NG2-specific CRH cKO and CTRL animals, $n_{TP/GT}$ = 5–6 mice.
(N and O) Representative images of Olig2/CC1 staining in CTRL (E) and cKO (F) animals. Scale bars, 50 μm, $n_{TP/GT}$ = 4–6 mice.
(P) Number of CC1$^+$/Olig2$^+$ in global CRHR1 KO and WT animals, $n_{TP/GT}$ = 4–6 mice.
(Q) Number of CC1$^-$/Olig2$^+$ cells in global CRHR1 KO and WT animals, $n_{TP/GT}$ = 4–6 mice.
(R) Number of Olig2$^+$ in global CRHR1 KO and WT animals, $n_{TP/GT}$ = 4–6 mice.
(S) % of CC1$^+$ cells of Olig2$^+$ cells in global CRHR1 KO and WT animals, $n_{TP/GT}$ = 4–6 mice.
(T and U) Representative images of CC1/Olig2 staining in CRHR1 WT (T) and KO (U) animals. Scale bars, 50 μm.
For all images, white arrowheads indicate cells or structures. Yellow arrowheads indicate co-localization of indicated markers. All data points represent individual animals. The *p* values are from one-way ANOVA (G and H) and two-way ANOVAs with Sidak's post hoc test (I–M, P–S), $^*p < 0.05$, $^{****}p < 0.0001$, data are shown as mean ± SEM.

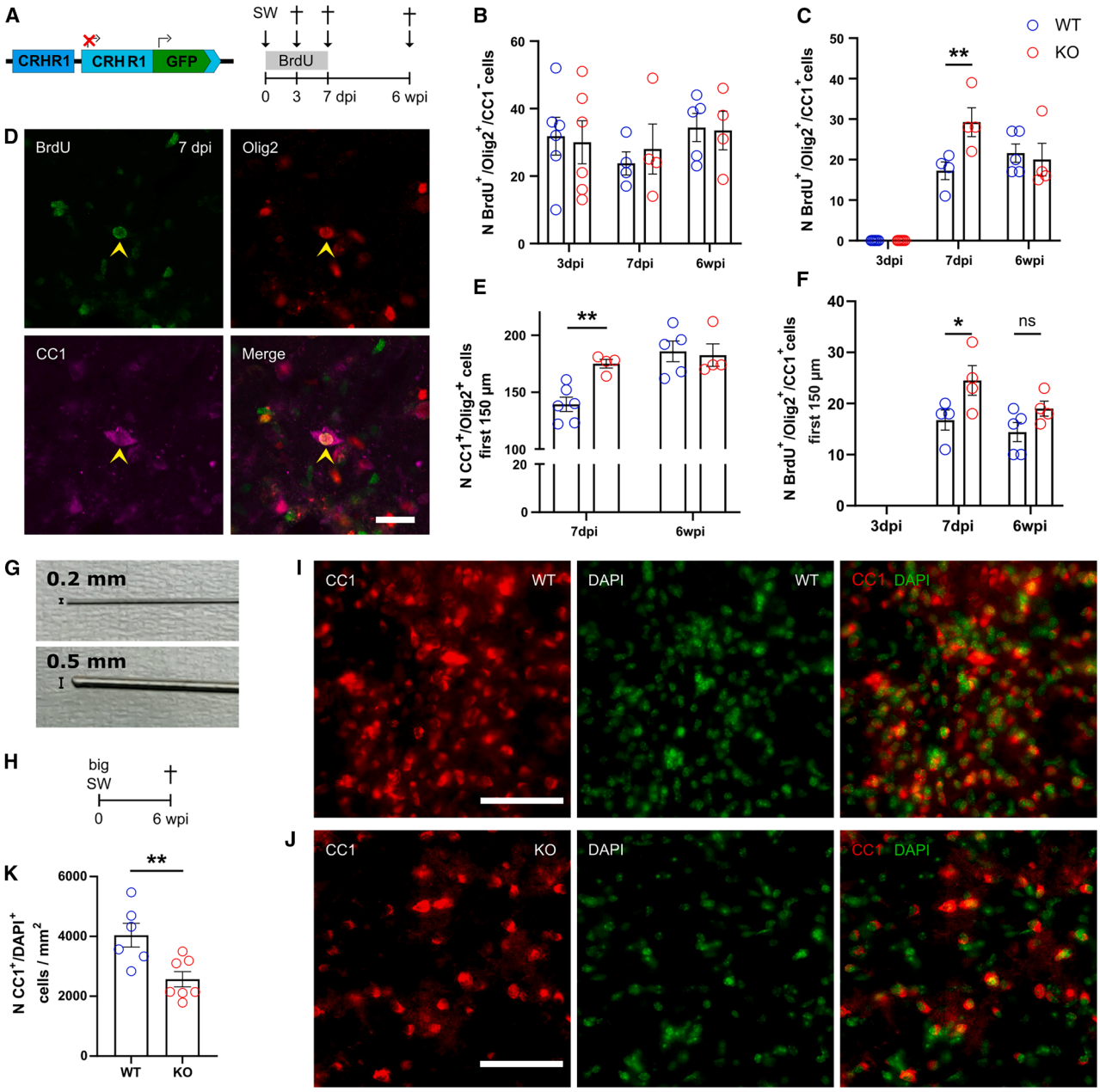

Figure 6. CRH/CRHR1 system regulates early differentiation and long term-survival after injury

(A) The *CRHR1*$^{\Delta EGFP}$ mouse model and experimental scheme.

(B) Quantification of BrdU$^+$/Olig2$^+$/CC1$^-$ cells in a 300-µm radius around injury site. $n_{TP/GT}$ = 5–6 animals.

(C) Quantification of BrdU$^+$/Olig2$^+$/CC1$^+$ cells around injury site, $n_{TP/GT}$ = 5–6 animals.

(D) Confocal image of BrdU/Olig2/CC1 staining at 7 dpi, $n_{TP/GT}$ = 5–6 animals.

(E and F) Quantification of CC1$^+$/Olig2$^+$ cells (E) and BrdU$^+$/CC1$^+$/Olig2$^+$ within 150 µm (F), $n_{TP/GT}$ = 5–6 animals.

(G) Binocular image of small (0.2 mm) and big (0.5 mm) Hamilton syringe.

(H) Experimental setup to test the influence of 2.5× increased injury size.

(I and J) Confocal images of CC1$^+$/DAPI$^+$ cells around the injury site in WT (I) and KO animals (J). Scale bars, 50 µm.

(K) Quantification of CC1$^+$/DAPI$^+$ cells/mm^2 in the first 50 µm around the injury site at 6 wpi, n_{GT} = 6–7 animals.

Yellow arrowheads indicate co-localization of indicated markers. All data points represent individual animals. The *p* values are from two-way ANOVAs with Sidak's post hoc test (B, C, E, F) and from two tailed Student's t-test, *$p < 0.05$, ****$p < 0.0001$, data are shown as mean ± SEM.

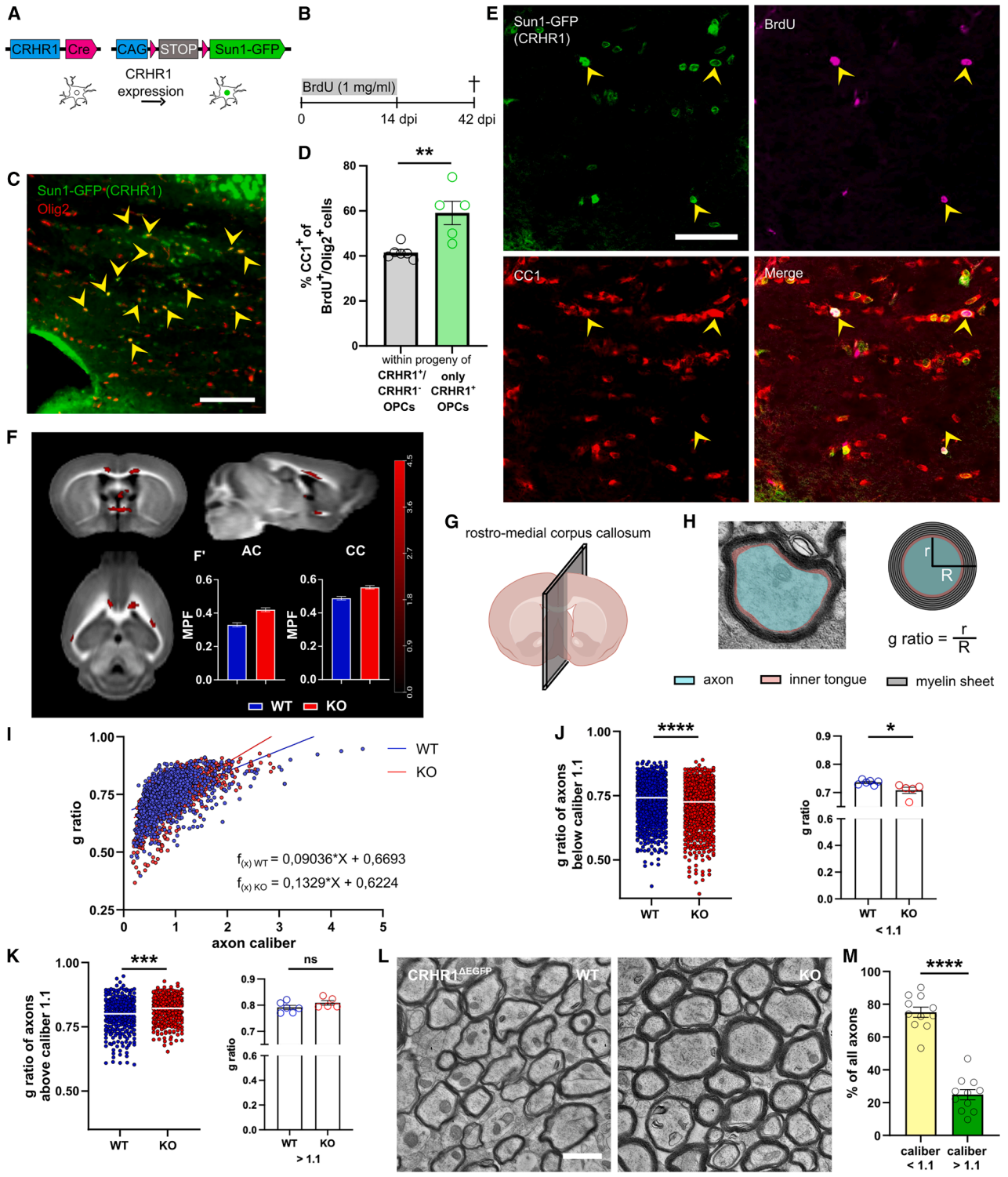

Figure 7. CRHR1$^+$ OLCs' population dynamics and CRHR1-dependent regulation of adult myelin

(A) The *CRHR1-Cre:Sun1-GFP* reporter mouse model.

(B) Label-retaining experiment using BrdU in *CRHR1-Cre::Sun1-GFP* mice to study OPC differentiation under non-injury conditions.

(C) Confocal images showing aggregation of Sun1-GFP$^+$ (CRHR1$^+$)/Olig2$^+$ cells in the CC. Scale bar, 50 μm.

(D) % CC1$^+$ of BrdU$^+$/Olig2$^+$ and all BrdU$^+$/Sun1-GFP$^+$ (CRHR1$^+$) cells at 42 dpi. *n* = 5 animals.

(E) Confocal images of CC1$^+$/BrdU$^+$/Sun1-GFP$^+$ (CRHR1$^+$) cells in the CC. Scale bar, 50 μm.

(legend continued on next page)

the increase in CRHR1$^+$ OLCs paralleled that of the overall OL population.[25] We quantified the total number of Olig2$^+$ cells and calculated the percentage of CRHR1$^+$/Olig2$^+$ cells, which indeed significantly increased in the WM and MB over time (Figures S7J and S7K). This increase in the proportion of CRHR1$^+$/Olig2$^+$ cells suggested that CRHR1$^+$ OLCs increased their number at a higher rate than the population of CRHR1$^-$ OLCs, implicating that the CRHR1$^+$ OPC subpopulation may play an important role in adult OL maturation and potentially also myelination.

Increased number of CRHR1-expressing OLCs under non-injury conditions is caused by an elevated differentiation rate

To further investigate the cause of the observed increase in CRHR1-expressing OLCs, we conducted a label-retaining experiment in *CRHR1-Cre::Sun1-GFP* mice by treating them with BrdU for 2 weeks, followed by a retaining phase of 4 weeks (Figures 7A and 7B). We then compared the differentiation rate of CRHR1-expressing OPCs to that of all OPCs in the CC (Figure 7C). Assessment of the percentage of CC1$^+$ cells in the population of formerly proliferating cells (OPCs) revealed a significantly higher percentage of differentiated cells in the CRHR1-expressing population (CRHR1$^+$: 59.09% ± 5.22%, all: 41.53% ± 1.28%) after the 4-week retaining period (Figures 7D and 7E). Combined with previous results following acute injury, this suggests that CRHR1 may act as an inhibitory regulator, preventing premature oligodendrogenesis under certain conditions, which is critical for adequate differentiation and thus long-term survival.

Inhibition of CRH/CRHR1 interaction under non-injury conditions leads to premature differentiation and long-lasting changes in the myelin structure

While CRH-expression in OPCs can only be observed following injury, neurons represent the major source of CRH under non-injury conditions. To test the effect of CRH/CRHR1 signaling in OPCs under non-injury conditions and its effect on oligodendrogenesis, we used *CRHR1$^{\Delta EGFP}$* mice. Because the main developmental oligodendrogenesis and myelination occurs during early postnatal stages,[26] we first sacrificed *CRHR1$^{\Delta EGFP}$* mice at postnatal day 8 (p8) and assessed the number of OLs in CRHR1 WT and KO animals (Figures S8A and S8B). Intriguingly, we found increased numbers of OLs in the central corpus callosum (CC) in CRHR1 KO mice (Figures S8C and S8D). This suggests that CRH/CRHR1 signaling inhibits premature oligodendrogenesis not only following injury but also during early postnatal development. Nevertheless, this premature oligodendrogenesis did not lead to an increase in the MBP signal in the corresponding area (Figure S8E), implying that the differences in the number of OLs were caused by premyelinating stages.

Next, we assessed whether this CRHR1 KO-dependent premature oligodendrogenesis also impacted on adult myelination patterns. We first conducted anti-MBP stainings on brain sections of adult *CRHR1$^{\Delta EGFP}$* animals and assessed OL numbers as well as potential intensity and coverage differences in the CX and WM. The analyses revealed that the MBP staining intensity was significantly increased in the CX of CRHR1 KO animals (WT: 1068 ± 69.36 MGV; KO: 1362 ± 32.44 MGV; Figures S8F and S8G). In the WM, MBP intensity differences were not detectable, likely due to the high default background intensity (data not shown). To overcome these intensity-connected drawbacks, we used magnetic resonance imaging (MRI) to measure myelin content differences more globally. A specific MRI method is the magnetization transfer (MT), which can be used to estimate the macromolecular proton fraction (MPF). MPF represents the most sensitive biomarker of myelin density in MRI and has been shown to be superior to other methods like diffusion tensor imaging-derived fractional anisotropy.[27–31] Comparison between CRHR1 WT and KO mice revealed significantly increased myelin content in various brain regions, including the medial and lateral CC and AC (Figures 7F and 7F′). To further understand the underlying differences in these myelin alterations and to get insight on potential structural differences in myelin, we performed electron microscopy (EM) of the rostro-medial CC of adult *CRHR1$^{\Delta EGFP}$* mice (Figure 7G). Analysis of the g ratio in relation to axon caliber showed significant differences in the linear regression slopes between WT and KO animals (Figures 7H and 7I). To better understand the differences in the g ratio in different axon calibers, we calculated the intersection point between the two regression curves. The calculated value of 1.1 μm was used to separate the axons in two populations, smaller or larger than an axon caliber of 1.1 μm. We then compared the average g ratio of axons smaller or larger than 1.1 μm between genotypes and found that smaller caliber axons in KO mice had a significantly smaller g ratio (thicker myelin; WT: 0.73 ± 0.0023; KO: 0.71 ± 0.0026), while larger caliber axons had a significantly increased g ratio (thinner myelin; WT: 0.80 ± 0.0036; KO: 0.82 ± 0.0028; Figures 7J and 7K).

To understand the impact of these g ratio changes on overall myelin content, we examined the distribution of axon calibers. We found that 75.15% ± 3.15% of axons had a caliber smaller than 1.1 μm, likely causing the net increase in myelin content observed in MRI data (Figures 7L and 7M). Because of this CRH/CRHR1 system-connected influence on myelin, we also tested whether active demyelination is able to induce the CRH/CRHR1 system. To this end, we treated *CRH-Cre::Ai9* mice

(F) Calculated T-contrast ($p_{FDR\ cluster} < 0.05$, collection threshold of $p < 0.01$) on brain matrix.
(F′) Plotted MPF peak voxel values in the AC and CC.
(G and H) g ratio analysis (with R = radius myelin sheath and r = radius axon).
(I) g ratio in dependence of axon caliber of WT and KO animals.
(J and K) g ratio of axon with caliber smaller (I) and bigger (J) than 1.1 μm for all axons separately ($n_{animals/GT}$ = 5–6) and per animal.
(L) EM image of myelinated axons in the medial CC in WT and KO animals. Scale bar, 1 μm.
(M) % of all axons with a caliber below and above 1.1 μm, n = 11 animals.
For all images, yellow arrowheads indicate co-localization of indicated markers. Data points represent individual animals (D and J, right; K, right; and M) or individual axons (I and J, left; and K, left). The p values are from two-tailed Student's t test (D and J, right; K, right; and M) and Mann-Whitney U test (J, left; and K, left), $^*p < 0.05$, $^{****}p < 0.0001$, data are shown as mean ± SEM.

with the demyelinating substance cuprizone (CPZ) for 6 weeks and analyzed whether CRH expression was triggered in OPCs (Figures S8H and S8I). Indeed, after 4 weeks of CPZ treatment, $CRH^+/CC1^+$ OLs were observed throughout the brains of treated mice (Figures S8J and S8K), suggesting an active role of this OPC subtype in the reaction to different injury conditions, including acute injury and demyelination. In summary, these findings demonstrate that CRH/CRHR1 signaling is not only activated under injury conditions but also plays an important role in regulating OL generation during early postnatal development, influences adult myelination patterns by increasing myelin sheath thickness of small caliber axons, and may contribute to regeneration following active demyelination.

DISCUSSION

Oligodendrogenesis and myelination are the primary functions of OPCs; however, not all mechanisms regulating these processes are fully understood. Neuropeptides such as CRH represent a large and diverse group of molecules typically considered as neuromodulators and have been implicated in a wide variety of processes in the CNS. So far, they have been investigated predominantly in the context of neuronal development and as modulators of synaptic transmission.[15,32,33]

In our study, we identified and characterized a novel CRH/CRHR1 system in the OL lineage. We found that this system modulates OPC differentiation and subsequent myelination following injury, as well as under physiological non-injury conditions. Initially, we discovered a subpopulation of CRH-expressing OPCs constituting 30% of the total population of injury-responsive OPCs. This contribution distinguishes them from other OPC subpopulations, such as the $GPR17^+$ OPCs, which only contribute ≈14% to the whole OPC population and underscores their potential impact on the general injury response.[34] CRH expression was observed to commence within 12 hpi, a finding confirmed by a published single-cell sequencing dataset.[35] The identification of CRH expression in OPCs represents not only the first comprehensive *in vivo* description of neuropeptide expression in OPCs but also one of the earliest reported responses of OPCs to acute injury. Although their population dynamics are similar to the general population of OPCs, CRH-expressing OPCs differ in their specific proliferative response as well as their differentiation tendency. Proliferation is markedly increased (100% proliferation rate) in this population compared to all OPCs responding to cortical injury (40%).[6]

Additionally, their high maturation rate of 80% distinguishes them from the general population of cortical OPCs, which have been reported to possess a relatively low oligodendrogenic potential.[4,6] These discrepancies were not caused by regional differences in the OPC population between the CX and MB, as shown by the comparison to other MB OPCs, which clearly highlights that CRH-expressing OPCs exhibit a faster and higher differentiation rate. Additionally, their significant role in injury-related recovery is emphasized by their extensive contribution to the population of newly generated OLs (≈40%) and their remarkable stability after integration, as evidenced by the persistence of OLs derived from CRH-expressing OPCs up to 4 months following acute injury.[25]

Given the absence of CRH-expressing OPCs in the brain under non-injury conditions, we first investigated their role in regenerative processes following injury. Our findings indicate that OPC-derived CRH delays the differentiation of another OPC subpopulation expressing CRHR1, thereby facilitating long-term survival of OLs. This hypothesis is supported by the identification of CRHR1-expressing OPCs surrounding the injury site, which also generate myelinating OLs. While CRHR1 expression in OPCs was confirmed on different levels in this study, its expression has also been identified in different sequencing studies, further strengthening our finding.[36–40] Following injury, we found that the dynamics of oligodendrogenesis in the $CRHR1^+$ OPC population are slower compared to the whole OPC population. Furthermore, NG2-specific CRH or global CRHR1 inactivation resulted in an increase in the differentiation velocity, leading to a long-lasting loss of OLs in an injury size-dependent manner. The absence of this effect on oligodendrogenesis in NG2-specific CRHR1 KO animals remains unclear. It may suggest that the TAM-induced recombination efficiency was insufficient to produce a comparable outcome. Additionally, the small number of $CRHR1^+$ astrocytes identified in close proximity of the injury site might also contribute to the observed effect. This indicates that, at least following injury, the impact on OLs might not be entirely cell autonomous. Nevertheless, CRHR1 in OPCs seems to act in a similar way as GPR17, which has also been identified as a modulator of OL generation velocity.[41] That premature differentiation can result in cellular loss before stable integration was already shown in other studies.[42] The necessity for the delay caused by CRH/CRHR1 interaction following injury may be related to the exposure to conditions of high oxidative stress present at early stages, which OLs, depending on their differentiation state, are particularly vulnerable to.[43] Evidence that an inflammatory environment can impact OPC differentiation was just recently provided in a study by *Meijer* et al., in which BCAS1 expression was epigenetically downregulated following treatment with interferon γ.[44] Besides, other studies have already shown that timing of cell-cycle exit, subsequent OPC differentiation, and initiation of maturation are tightly regulated by different factors.[41,45,46] It remains unclear why CRH-expressing OPCs seem to be less vulnerable to this environment and only prevent CRHR1-expressing OPCs from premature differentiation. One hypothesis is that there are intrinsic differences between the different OPC subpopulations that go beyond their expression of CRH and CRHR1. This is further indicated by the fact that CRH-expressing OPCs only occur under injury or demyelinating, but not under physiological conditions, whereas CRHR1-expressing OPCs are already present under baseline conditions. This raises the question of additional triggers of CRH-expression in OPCs but also for other sources of CRH, e.g., neurons, that might influence CRHR1-expressing OPCs and OLs.

When assessing the population dynamics of CRHR1-expressing OPCs under non-injury conditions, we found that they exhibited a significantly higher capacity for differentiation compared to other OPCs. Hence, when serving the same transient inhibitory purpose under physiological conditions as following injury, the inactivation of CRHR1 was suspected to further increase their oligodendrogenic potential. Indeed, we

found that CRHR1 ablation led to premature differentiation at early postnatal timepoints, without a parallel increase in myelination. Nevertheless, increased adult myelination, as evidenced by anti-MBP staining, MRI-based myelin assessment, and EM, suggests that the accelerated generation rate directly affects long-term myelination. The increase in the total amount of myelin was accompanied by a shift in the myelination pattern, with thicker myelin in small-caliber axons and thinner in large-caliber axons. This observation points in the direction that, although OLs seemingly myelinate small-caliber axons prematurely and to a greater extent, their ability to myelinate large-caliber axons is impaired. This may reflect a compensatory mechanism aimed at restoring physiological conduction velocity. While CRHR1 inactivation affects oligodendrogenesis following acute injury without altering myelination, it leads to myelination differences under physiological conditions. Furthermore, activation of the CRH/CRHR1 system in OPCs following CPZ treatment underscores the need for further investigation into its role in remyelination. The impact of CRH either from OPC or non-OPC sources during developmental and adult myelination remains elusive but might be connected to its physiological role as a stress-responsive neuropeptide.[47,48] Previous studies have shown that stress, particularly during the early postnatal phase, can disrupt oligodendrogenesis, leading to long-lasting effects on both myelin structure and animal behavior.[49–54] It is intriguing to speculate that the behavioral phenotype observed in constitutive CRHR1 KO mice may, to some extent, be influenced by the myelination difference identified in this study.[55,56] Given that CRH is widely recognized as a stress peptide involved in stress-related pathologies, further exploring its impact on the CRH/CRHR1 system in OPCs is a natural direction for future research.[3] The fact that neuropeptides, unlike fast-acting neurotransmitters, possess slow-release kinetics and primarily act through GPCRs via volume transmission makes them ideally suited to modulate long-lasting effects on myelination.[15,57]

Ultimately, this study reveals (1) a previously unknown, context-dependent secretory response of the neuropeptide CRH by OPCs; (2) its direct impact on the oligodendrogenic potential of a distinct subpopulation of CRHR1-expressing OPCs; and (3) that CRHR1-expressing OPCs—regardless of the CRH source—exhibit an increased oligodendrogenic tendency, which is further amplified by CRHR1 inactivation, leading to alterations in myelin structure. Together, these findings suggest that CRH—and potentially other neuropeptides—can significantly influence oligodendrogenesis and myelination under both physiological and pathological conditions.

Limitations of the study

In this study, we identify a novel CRH/CRHR1 signaling axis in OLCs that regulates OPC differentiation and myelination. Although key aspects were elucidated, several limitations remain. The cell-autonomous role of CRHR1 signaling in OPCs could not be conclusively demonstrated, likely due to incomplete recombination in the tamoxifen-inducible *CRHR1*$^{NG2\text{-}cKO}$ model. Employing a constitutive OPC-specific Cre line may overcome this limitation and better clarify the intrinsic function of CRHR1 in the OL lineage. Additionally, it should be noted that *CRHR1*$^{\Delta EGFP}$ mice—similar to other CRHR1 knockout models—display reduced corticosterone levels, which may have attenuated CRH/CRHR1 effects. The role of CRHR1 in remyelination also remains unresolved, as this was not the primary focus in the stab-wound model. While OL survival is affected, long-term myelination appears preserved. Expanding the cuprizone experiments and employing OPC-specific CRH and CRHR1 knockouts will be necessary to resolve this discrepancy.

RESOURCE AVAILABILITY

Lead contact

Requests for further information and resources should be directed to and will be fulfilled by the lead contact, Jan M. Deussing (deussing@psych.mpg.de).

Materials availability

This study did not generate new reagents.

Data and code availability

- Additional data supporting the findings of this study are available from the corresponding authors upon reasonable request.
- All used code and macros used in this study are available from the corresponding authors upon reasonable request.
- All additional information is available from the corresponding authors upon reasonable request.

ACKNOWLEDGMENTS

The authors thank Sabrina Bauer and Stefanie Unkmeir for their assistance with genotyping, Andrea Parl for her constant assistance in the lab, and Elfi Fesl for proofreading the manuscript. We thank Sandra Goebbels for her scientific input and for sharing different antibodies with us. Additionally, we thank Mathias Schmidt for providing AAV1/2-CMV-DIO-eGFP virus. Two icons (Figures 3A and 7G) were created with BioRender.com. The project was supported by the Max Planck Society (JMD). C.R. received funding from the International Max Planck Research School for Translational Psychiatry and the Gunter Sachs Donation.

AUTHOR CONTRIBUTIONS

C.R. designed, led, and performed all experiments; analyzed and interpreted data; and wrote the manuscript. T.S., B.B., and M.C. performed MRI measurements and analyses, provided essential scientific input, and subedited the manuscript. T.R., W.M., and K.-A.N. acquired EM pictures, provided essential scientific input on image analysis, and subedited the manuscript. J.P.D. and D.B.N. provided material, performed tissue expansion and subsequent staining, and subedited the manuscript. A.M.I. and L.D. performed immunostainings and analyses, provided essential scientific input, and subedited the manuscript. J.T.v.P. analyzed data and subedited the manuscript. A.U. and A.A. helped with cannula implantations and image acquisition at the 2-photon setup, provided essential scientific input, and subedited the manuscript. S.C. and I.-A.v.M.H. aided with methodological and scientific expertise. K.S. and K.I. created and provided the CRH-Venus mouse line and reviewed the manuscript. J.M.D. provided essential scientific advice and support, supervised all experiments and analyses, and reviewed and edited the manuscript.

DECLARATION OF INTERESTS

The authors declare no competing interests.

STAR★METHODS

Detailed methods are provided in the online version of this paper and include the following:

- KEY RESOURCES TABLE
- EXPERIMENTAL MODEL AND STUDY PARTICIPANT DETAILS

- METHOD DETAILS
  - Stereotaxic surgeries
  - Acute injury for CRH$^+$ OLC quantification and modulation experiments
  - Injection of fluorescent bead and viruses
  - Cranial window implantation with injury infliction
  - Implantation of subcortical imaging cannula
  - In-vivo 2-photon imaging
  - Magnetic resonance imaging (MRI)
  - Magnetization transfer (MT) to assess molecular proton fraction (MPF)
  - Experimental setup for modulation of CRH/CRHR1 system in glial cells
  - Quantification of CD31$^+$ vascularization
  - Label retaining experiment
  - Cryosectioning
  - Immunofluorescence staining
  - Expansion microscopy
  - Image acquisition
  - Quantification of CRH-expressing OPCs in *CRH-Cre::Ai9* mice
  - Quantification of CRHR1-expressing OLCs at 1.5, 3 and 5 months in *CRHR1-Cre::LSL-FlpO::Ai9* mice
  - Quantification of cells in CRH/CRHR1 system modulation experiments
  - MRI analysis
  - Electron microscopy
  - G ratio measurement and analysis
- QUANTIFICATION AND STATISTICAL ANALYSIS

SUPPLEMENTAL INFORMATION

Supplemental information can be found online at https://doi.org/10.1016/j.celrep.2025.116474.

Received: January 25, 2025
Revised: June 10, 2025
Accepted: October 3, 2025

REFERENCES

1. Raff, M.C., Miller, R.H., and Noble, M. (1983). A glial progenitor cell that develops in vitro into an astrocyte or an oligodendrocyte depending on culture medium. Nature *303*, 390–396. https://doi.org/10.1038/303390a0.
2. Jakel, S., and Dimou, L. (2017). Glial Cells and Their Function in the Adult Brain: A Journey through the History of Their Ablation. Front. Cell. Neurosci. *11*, 24. https://doi.org/10.3389/fncel.2017.00024.
3. Nishiyama, A., Serwanski, D.R., and Pfeiffer, F. (2021). Many roles for oligodendrocyte precursor cells in physiology and pathology. Neuropathology *41*, 161–173. https://doi.org/10.1111/neup.12732.
4. Dimou, L., Simon, C., Kirchhoff, F., Takebayashi, H., and Götz, M. (2008). Progeny of Olig2-expressing progenitors in the gray and white matter of the adult mouse cerebral cortex. J. Neurosci. *28*, 10434–10442. https://doi.org/10.1523/JNEUROSCI.2831-08.2008.
5. Vigano, F., Schneider, S., Cimino, M., Bonfanti, E., Gelosa, P., Sironi, L., Abbracchio, M.P., and Dimou, L. (2016). GPR17 expressing NG2-Glia: Oligodendrocyte progenitors serving as a reserve pool after injury. Glia *64*, 287–299. https://doi.org/10.1002/glia.22929.
6. von Streitberg, A., Jäkel, S., Eugenin von Bernhardi, J., Straube, C., Buggenthin, F., Marr, C., and Dimou, L. (2021). NG2-Glia Transiently Overcome Their Homeostatic Network and Contribute to Wound Closure After Brain Injury. Front. Cell Dev. Biol. *9*, 662056. https://doi.org/10.3389/fcell.2021.662056.
7. Hughes, E.G., Kang, S.H., Fukaya, M., and Bergles, D.E. (2013). Oligodendrocyte progenitors balance growth with self-repulsion to achieve homeostasis in the adult brain. Nat. Neurosci. *16*, 668–676. https://doi.org/10.1038/nn.3390.
8. Simon, C., Götz, M., and Dimou, L. (2011). Progenitors in the adult cerebral cortex: cell cycle properties and regulation by physiological stimuli and injury. Glia *59*, 869–881. https://doi.org/10.1002/glia.21156.
9. Trapp, B.D., Nishiyama, A., Cheng, D., and Macklin, W. (1997). Differentiation and Death of Premyelinating Oligodendrocytes in Developing Rodent Brain. J. Cell Biol. *137*, 459–468. https://doi.org/10.1083/jcb.137.2.459.
10. Hughes, E.G., Orthmann-Murphy, J.L., Langseth, A.J., and Bergles, D.E. (2018). Myelin remodeling through experience-dependent oligodendrogenesis in the adult somatosensory cortex. Nat. Neurosci. *21*, 696–706. https://doi.org/10.1038/s41593-018-0121-5.
11. Barres, B.A., Hart, I.K., Coles, H.S., Burne, J.F., Voyvodic, J.T., Richardson, W.D., and Raff, M.C. (1992). Cell-Death and Control of Cell-Survival in the Oligodendrocyte Lineage. Cell *70*, 31–46. https://doi.org/10.1016/0092-8674(92)90531-G.
12. Hughes, E.G., and Stockton, M.E. (2021). Premyelinating Oligodendrocytes: Mechanisms Underlying Cell Survival and Integration. Front. Cell Dev. Biol. *9*, 714169. https://doi.org/10.3389/fcell.2021.714169.
13. Gibson, E.M., Purger, D., Mount, C.W., Goldstein, A.K., Lin, G.L., Wood, L.S., Inema, I., Miller, S.E., Bieri, G., Zuchero, J.B., et al. (2014). Neuronal Activity Promotes Oligodendrogenesis and Adaptive Myelination in the Mammalian Brain. Science *344*, 1252304. https://doi.org/10.1126/science.1252304.
14. Osso, L.A., Rankin, K.A., and Chan, J.R. (2021). Experience-dependent myelination following stress is mediated by the neuropeptide dynorphin. Neuron *109*, 3619–3632.e5. https://doi.org/10.1016/j.neuron.2021.08.015.
15. van den Pol, A.N. (2012). Neuropeptide transmission in brain circuits. Neuron *76*, 98–115. https://doi.org/10.1016/j.neuron.2012.09.014.
16. Ozcete, O.D., Banerjee, A., and Kaeser, P.S. (2024). Mechanisms of neuromodulatory volume transmission. Mol. Psychiatry *29*, 3680–3693. https://doi.org/10.1038/s41380-024-02608-3.
17. Joels, M., and Baram, T.Z. (2009). OPINION The neuro-symphony of stress. Nat. Rev. Neurosci. *10*, 459–U484. https://doi.org/10.1038/nrn2632.
18. Deussing, J.M., and Chen, A. (2018). The Corticotropin-Releasing Factor Family: Physiology of the Stress Response. Physiol. Rev. *98*, 2225–2286. https://doi.org/10.1152/physrev.00042.2017.
19. Stevens, S.L., Shaw, T.E., Dykhuizen, E., Lessov, N.S., Hill, J.K., Wurst, W., and Stenzel-Poore, M.P. (2003). Reduced cerebral injury in CRH-R1 deficient mice after focal ischemia: a potential link to microglia and atrocytes that express CRH-R1. J. Cereb. Blood Flow Metab. *23*, 1151–1159. https://doi.org/10.1097/01.WCB.0000086957.72078.D4.
20. de la Tremblaye, P.B., Benoit, S.M., Schock, S., and Plamondon, H. (2017). CRHR1 exacerbates the glial inflammatory response and alters BDNF/TrkB/pCREB signaling in a rat model of global cerebral ischemia: implications for neuroprotection and cognitive recovery. Prog. Neuropsychopharmacol. Biol. Psychiatry *79*, 234–248. https://doi.org/10.1016/j.pnpbp.2017.06.021.
21. Kono, J., Konno, K., Talukder, A.H., Fuse, T., Abe, M., Uchida, K., Horio, S., Sakimura, K., Watanabe, M., and Itoi, K. (2017). Distribution of corticotropin-releasing factor neurons in the mouse brain: a study using corticotropin-releasing factor-modified yellow fluorescent protein knock-in mouse. Brain Struct. Funct. *222*, 1705–1732. https://doi.org/10.1007/s00429-016-1303-0.
22. Chen, F., Tillberg, P.W., and Boyden, E.S. (2015). Expansion microscopy. Science *347*, 543–548. https://doi.org/10.1126/science.1260088.
23. Delling, J.P., Bauer, H.F., Gerlach-Arbeiter, S., Schön, M., Jacob, C., Wagner, J., Pedro, M.T., Knöll, B., and Boeckers, T.M. (2024). Combined expansion and STED microscopy reveals altered fingerprints of postsynaptic nanostructure across brain regions in ASD-related SHANK3-deficiency. Mol. Psychiatry *29*, 2997–3009. https://doi.org/10.1038/s41380-024-02559-9.

24. Refojo, D., Schweizer, M., Kuehne, C., Ehrenberg, S., Thoeringer, C., Vogl, A.M., Dedic, N., Schumacher, M., von Wolff, G., Avrabos, C., et al. (2011). Glutamatergic and Dopaminergic Neurons Mediate Anxiogenic and Anxiolytic Effects of CRHR1. Science *333*, 1903–1907. https://doi.org/10.1126/science.1202107.

25. Tripathi, R.B., Jackiewicz, M., McKenzie, I.A., Kougioumtzidou, E., Grist, M., and Richardson, W.D. (2017). Remarkable Stability of Myelinating Oligodendrocytes in Mice. Cell Rep. *21*, 316–323. https://doi.org/10.1016/j.celrep.2017.09.050.

26. de Faria, O., Pivonkova, H., Varga, B., Timmler, S., Evans, K.A., and Káradóttir, R.T. (2021). Periods of synchronized myelin changes shape brain function and plasticity. Nat. Neurosci. *24*, 1508–1521. https://doi.org/10.1038/s41593-021-00917-2.

27. Yarnykh, V.L. (2012). Fast macromolecular proton fraction mapping from a single off-resonance magnetization transfer measurement. Magn. Reson. Med. *68*, 166–178. https://doi.org/10.1002/mrm.23224.

28. Yarnykh, V.L. (2016). Time-efficient, high-resolution, whole brain three-dimensional macromolecular proton fraction mapping. Magn. Reson. Med. *75*, 2100–2106. https://doi.org/10.1002/mrm.25811.

29. Khodanovich, M.Y., Sorokina, I.V., Glazacheva, V.Y., Akulov, A.E., Nemirovich-Danchenko, N.M., Romashchenko, A.V., Tolstikova, T.G., Mustafina, L.R., and Yarnykh, V.L. (2017). Histological validation of fast macromolecular proton fraction mapping as a quantitative myelin imaging method in the cuprizone demyelination model. Sci. Rep. *7*, 46686. https://doi.org/10.1038/srep46686.

30. Soustelle, L., Antal, M.C., Lamy, J., Harsan, L.-A., and Loureiro de Sousa, P. (2021). Determination of optimal parameters for 3D single-point macromolecular proton fraction mapping at 7T in healthy and demyelinated mouse brain. Magn. Reson. Med. *85*, 369–379. https://doi.org/10.1002/mrm.28397.

31. Hertanu, A., Soustelle, L., Buron, J., Le Priellec, J., Cayre, M., Le Troter, A., Prevost, V.H., Ranjeva, J.P., Varma, G., Alsop, D.C., et al. (2023). Inhomogeneous Magnetization Transfer (ihMT) imaging in the acute cuprizone mouse model of demyelination/remyelination. Neuroimage *265*, 119785. https://doi.org/10.1016/j.neuroimage.2022.119785.

32. Russo, A.F. (2017). Overview of Neuropeptides: Awakening the Senses? Headache *57*, 37–46. https://doi.org/10.1111/head.13084.

33. Guillaumin, M.C.C., and Burdakov, D. (2021). Neuropeptides as Primary Mediators of Brain Circuit Connectivity. Front. Neurosci. *15*, 644313. https://doi.org/10.3389/fnins.2021.644313.

34. Miralles, A.J., Unger, N., Kannaiyan, N., Rossner, M.J., and Dimou, L. (2023). Analysis of the GPR17 receptor in NG2-glia under physiological conditions unravels a new subset of oligodendrocyte progenitor cells with distinct functions. Glia *71*, 1536–1552. https://doi.org/10.1002/glia.24356.

35. Li, C., Wu, Z., Zhou, L., Shao, J., Hu, X., Xu, W., Ren, Y., Zhu, X., Ge, W., Zhang, K., et al. (2022). Temporal and spatial cellular and molecular pathological alterations with single-cell resolution in the adult spinal cord after injury. Signal Transduct. Target. Ther. *7*, 65. https://doi.org/10.1038/s41392-022-00885-4.

36. Zhang, Y., Chen, K., Sloan, S.A., Bennett, M.L., Scholze, A.R., O'Keeffe, S., Phatnani, H.P., Guarnieri, P., Caneda, C., Ruderisch, N., et al. (2014). An RNA-Sequencing Transcriptome and Splicing Database of Glia, Neurons, and Vascular Cells of the Cerebral Cortex. J. Neurosci. *34*, 11929–11947. https://doi.org/10.1523/Jneurosci.1860-14.2014.

37. Zeisel, A., Hochgerner, H., Lönnerberg, P., Johnsson, A., Memic, F., van der Zwan, J., Häring, M., Braun, E., Borm, L.E., La Manno, G., et al. (2018). Molecular Architecture of the Mouse Nervous System. Cell *174*, 999–1014.e22. https://doi.org/10.1016/j.cell.2018.06.021.

38. Zeisel, A., Muñoz-Manchado, A.B., Codeluppi, S., Lönnerberg, P., La Manno, G., Juréus, A., Marques, S., Munguba, H., He, L., Betsholtz, C., et al. (2015). Cell types in the mouse cortex and hippocampus revealed by single-cell RNA-seq. Science *347*, 1138–1142. https://doi.org/10.1126/science.aaa1934.

39. Brown, T.I., Carr, V.A., LaRocque, K.F., Favila, S.E., Gordon, A.M., Bowles, B., Bailenson, J.N., and Wagner, A.D. (2016). Oligodendrocyte heterogeneity in the mouse juvenile and adult central nervous system. Science *352*, 1323–1326. https://doi.org/10.1126/science.aaf0784.

40. Falcao, A.M., van Bruggen, D., Marques, S., Meijer, M., Jakel, S., Agirre, E., Samudyata, S., Floriddia, E.M., Vanichkina, D., Ffrench-Constant, C., et al. (2019). Disease-specific oligodendrocyte lineage cells arise in Multiple Sclerosis. Glia *67*, E79.

41. Chen, Y., Wu, H., Wang, S., Koito, H., Li, J., Ye, F., Hoang, J., Escobar, S.S., Gow, A., Arnett, H.A., et al. (2009). The oligodendrocyte-specific G protein-coupled receptor GPR17 is a cell-intrinsic timer of myelination. Nat. Neurosci. *12*, 1398–1406. https://doi.org/10.1038/nn.2410.

42. Genoud, S., Lappe-Siefke, C., Goebbels, S., Radtke, F., Aguet, M., Scherer, S.S., Suter, U., Nave, K.A., and Mantei, N. (2002). Notch1 control of oligodendrocyte differentiation in the spinal cord. J. Cell Biol. *158*, 709–718. https://doi.org/10.1083/jcb.200202002.

43. Back, S.A., Gan, X., Li, Y., Rosenberg, P.A., and Volpe, J.J. (1998). Maturation-dependent vulnerability of oligodendrocytes to oxidative stress-induced death caused by glutathione depletion. J. Neurosci. *18*, 6241–6253. https://doi.org/10.1523/jneurosci.18-16-06241.1998.

44. Meijer, M., Agirre, E., Kabbe, M., van Tuijn, C.A., Heskol, A., Zheng, C., Mendanha Falcão, A., Bartosovic, M., Kirby, L., Calini, D., et al. (2022). Epigenomic priming of immune genes implicates oligodendroglia in multiple sclerosis susceptibility. Neuron *110*, 1193–1210.e13. https://doi.org/10.1016/j.neuron.2021.12.034.

45. Barres, B.A., Lazar, M.A., and Raff, M.C. (1994). A novel role for thyroid hormone, glucocorticoids and retinoic acid in timing oligodendrocyte development. Development *120*, 1097–1108.

46. Palazuelos, J., Klingener, M., and Aguirre, A. (2014). TGFβ Signaling Regulates the Timing of CNS Myelination by Modulating Oligodendrocyte Progenitor Cell Cycle Exit through SMAD3/4/FoxO1/Sp1. J. Neurosci. *34*, 7917–7930. https://doi.org/10.1523/jneurosci.0363-14.2014.

47. Peng, J., Long, B., Yuan, J., Peng, X., Ni, H., Li, X., Gong, H., Luo, Q., and Li, A. (2017). A Quantitative Analysis of the Distribution of CRH Neurons in Whole Mouse Brain. Front. Neuroanat. *11*, 63. https://doi.org/10.3389/fnana.2017.00063.

48. Chang, S., Fermani, F., Lao, C.-L., Huang, L., Jakovcevski, M., Giaimo, R.D., Gagliardi, M., Menegaz, D., Hennrich, A.A., Ziller, M., et al. (2022). Tripartite extended amygdala - basal ganglia CRH circuit drives arousal and avoidance behaviour. Preprint at: bioRxiv. https://doi.org/10.1101/2022.03.15.484057

49. Bordner, K., Au, E., Carlyle, B., Duque, A., Kitchen, R., Lam, T., Colangelo, C., Stone, K., Abbott, T., Mane, S., et al. (2011). Functional Genomic and Proteomic Analysis Reveals Disruption of Myelin-Related Genes and Translation in a Mouse Model of Early Life Neglect. Front. Psychiatry *2*, 18. https://doi.org/10.3389/fpsyt.2011.00018.

50. Teissier, A., Le Magueresse, C., Olusakin, J., Andrade da Costa, B.L.S., De Stasi, A.M., Bacci, A., Imamura Kawasawa, Y., Vaidya, V.A., and Gaspar, P. (2020). Early-life stress impairs postnatal oligodendrogenesis and adult emotional behaviour through activity-dependent mechanisms. Mol. Psychiatry *25*, 1159–1174. https://doi.org/10.1038/s41380-019-0493-2.

51. Yang, Y., Cheng, Z., Tang, H., Jiao, H., Sun, X., Cui, Q., Luo, F., Pan, H., Ma, C., and Li, B. (2017). Neonatal Maternal Separation Impairs Prefrontal Cortical Myelination and Cognitive Functions in Rats Through Activation of Wnt Signaling. Cereb. Cortex *27*, 2871–2884. https://doi.org/10.1093/cercor/bhw121.

52. Bonnefil, V., Dietz, K., Amatruda, M., Wentling, M., Aubry, A.V., Dupree, J.L., Temple, G., Park, H.J., Burghardt, N.S., Casaccia, P., and Liu, J. (2019). Region-specific myelin differences define behavioral consequences of chronic social defeat stress in mice. eLife *8*, e40855. https://doi.org/10.7554/eLife.40855.

53. Breton, J.M., Barraza, M., Hu, K.Y., Frias, S.J., Long, K.L.P., and Kaufer, D. (2021). Juvenile exposure to acute traumatic stress leads to long-lasting

alterations in grey matter myelination in adult female but not male rats. Neurobiol. Stress *14*, 100319. https://doi.org/10.1016/j.ynstr.2021.100319.

54. Raabe, F.J., Slapakova, L., Rossner, M.J., Cantuti-Castelvetri, L., Simons, M., Falkai, P.G., and Schmitt, A. (2019). Oligodendrocytes as A New Therapeutic Target in Schizophrenia: From Histopathological Findings to Neuron-Oligodendrocyte Interaction. Cells *8*, 1496. https://doi.org/10.3390/cells8121496.

55. Smith, G.W., Aubry, J.M., Dellu, F., Contarino, A., Bilezikjian, L.M., Gold, L. H., Chen, R., Marchuk, Y., Hauser, C., Bentley, C.A., et al. (1998). Corticotropin releasing factor receptor 1-deficient mice display decreased anxiety, impaired stress response, and aberrant neuroendocrine development. Neuron *20*, 1093–1102. https://doi.org/10.1016/s0896-6273(00)80491-2.

56. Timpl, P., Spanagel, R., Sillaber, I., Kresse, A., Reul, J.M., Stalla, G.K., Blanquet, V., Steckler, T., Holsboer, F., and Wurst, W. (1998). Impaired stress response and reduced anxiety in mice lacking a functional corticotropin-releasing hormone receptor 1. Nat. Genet. *19*, 162–166. https://doi.org/10.1038/520.

57. Fields, R.D. (2004). Volume transmission in activity-dependent regulation of myelinating glia. Neurochem. Int. *45*, 503–509. https://doi.org/10.1016/j.neuint.2003.11.015.

58. Meschkat, M., Steyer, A.M., Weil, M.T., Kusch, K., Jahn, O., Piepkorn, L., Agüi-Gonzalez, P., Phan, N.T.N., Ruhwedel, T., Sadowski, B., et al. (2022). White matter integrity in mice requires continuous myelin synthesis at the inner tongue. Nat. Commun. *13*, 1163. https://doi.org/10.1038/s41467-022-28720-y.

59. Taniguchi, H., He, M., Wu, P., Kim, S., Paik, R., Sugino, K., Kvitsiani, D., Fu, Y., Lu, J., Lin, Y., et al. (2011). A Resource of Cre Driver Lines for Genetic Targeting of GABAergic Neurons in Cerebral Cortex. Neuron *71*, 995. https://doi.org/10.1016/j.neuron.2011.12.010.

60. Salimando, G.J., Hyun, M., Boyt, K.M., and Winder, D.G. (2020). BNST GluN2D-Containing NMDA Receptors Influence Anxiety- and Depressive-like Behaviors and Modulate Cell-Specific Excitatory/Inhibitory Synaptic Balance. J. Neurosci. *40*, 3949–3968. https://doi.org/10.1523/Jneurosci.0270-20.2020.

61. Dedic, N., Kühne, C., Jakovcevski, M., Hartmann, J., Genewsky, A.J., Gomes, K.S., Anderzhanova, E., Pöhlmann, M.L., Chang, S., Kolarz, A., et al. (2018). Chronic CRH depletion from GABAergic, long-range projection neurons in the extended amygdala reduces dopamine release and increases anxiety. Nat. Neurosci. *21*, 803–807. https://doi.org/10.1038/s41593-018-0151-z.

62. Pivetta, C., Esposito, M.S., Sigrist, M., and Arber, S. (2014). Motor-Circuit Communication Matrix from Spinal Cord to Brainstem Neurons Revealed by Developmental Origin. Cell *156*, 537–548. https://doi.org/10.1016/j.cell.2013.12.014.

63. Zhu, X., Hill, R.A., Dietrich, D., Komitova, M., Suzuki, R., and Nishiyama, A. (2011). Age-dependent fate and lineage restriction of single NG2 cells. Development *138*, 745–753. https://doi.org/10.1242/dev.047951.

64. Madisen, L., Zwingman, T.A., Sunkin, S.M., Oh, S.W., Zariwala, H.A., Gu, H., Ng, L.L., Palmiter, R.D., Hawrylycz, M.J., Jones, A.R., et al. (2010). A robust and high-throughput Cre reporting and characterization system for the whole mouse brain. Nat. Neurosci. *13*, 133–140. https://doi.org/10.1038/nn.2467.

65. Mo, A., Mukamel, E.A., Davis, F.P., Luo, C., Henry, G.L., Picard, S., Urich, M.A., Nery, J.R., Sejnowski, T.J., Lister, R., et al. (2015). Epigenomic Signatures of Neuronal Diversity in the Mammalian Brain. Neuron *86*, 1369–1384. https://doi.org/10.1016/j.neuron.2015.05.018.

66. Madisen, L., Garner, A.R., Shimaoka, D., Chuong, A.S., Klapoetke, N.C., Li, L., van der Bourg, A., Niino, Y., Egolf, L., Monetti, C., et al. (2015). Transgenic Mice for Intersectional Targeting of Neural Sensors and Effectors with High Specificity and Performance. Neuron *85*, 942–958. https://doi.org/10.1016/j.neuron.2015.02.022.

67. Kuhne, C., Puk, O., Graw, J., de Angelis, M.H., Schutz, G., Wurst, W., and Deussing, J.M. (2012). Visualizing Corticotropin-Releasing Hormone Receptor Type 1 Expression and Neuronal Connectivities in the Mouse Using a Novel Multifunctional Allele. J. Comp. Neurol. *520*, 3150–3180. https://doi.org/10.1002/cne.23082.

68. Ulivi, A.F., Castello-VValdow, T.P., Weston, G., Yan, L., Yasuda, R., Chen, A., and Attardo, A. (2019). Longitudinal Two-Photon Imaging of Dorsal Hippocampal CA1 in Live Mice. J. Vis. Exp. *19*. https://doi.org/10.3791/59598.

69. Yarnykh, V.L. (2007). Actual flip-angle imaging in the pulsed steady state: a method for rapid three-dimensional mapping of the transmitted radiofrequency field. Magn. Reson. Med. *57*, 192–200. https://doi.org/10.1002/mrm.21120.

70. Hertanu, A., Soustelle, L., Le Troter, A., Buron, J., Le Priellec, J., Carvalho, V.N.D., Cayre, M., Durbec, P., Varma, G., Alsop, D.C., et al. (2022). T1D-weighted ihMT imaging – Part I. Isolation of long- and short-T1D components by T1D-filtering. Magn. Reson. Med. *87*, 2313–2328. https://doi.org/10.1002/mrm.29139.

71. Soustelle, L., Lamy, J., Le Troter, A., Hertanu, A., Guye, M., Ranjeva, J.-P., Varma, G., Alsop, D.C., Pelletier, J., Girard, O., and Duhamel, G. (2020). A Motion Correction Strategy for Multi-Contrast based 3D parametric imaging: Application to Inhomogeneous Magnetization Transfer (ihMT). Preprint at bioRxiv. https://doi.org/10.1101/2020.09.11.292649.

72. Damstra, H.G.J., Mohar, B., Eddison, M., Akhmanova, A., Kapitein, L.C., and Tillberg, P.W. (2022). Visualizing cellular and tissue ultrastructure using Ten-fold Robust Expansion Microscopy (TREx). eLife *11*, e73775. https://doi.org/10.7554/eLife.73775.

73. Weil, M.T., Ruhwedel, T., Meschkat, M., Sadowski, B., and Möbius, W. (2019). Transmission Electron Microscopy of Oligodendrocytes and Myelin. Methods Mol. Biol. *1936*, 343–375. https://doi.org/10.1007/978-1-4939-9072-6_20.

STAR★METHODS

KEY RESOURCES TABLE

REAGENT or RESOURCE	SOURCE	IDENTIFIER
Antibodies		
Rabbit anti NG2	Merck	Cat #: AB5320; RRID:AB_91789
Rabbit anti Olig2	Merck	Cat #: AB9610; RRID:AB_570666
Mouse anti Olig2	Merck	Cat #: MABN50; RRID:AB_10807410
Mouse anti APC (CC1)	Merck	Cat #: OP80; RRID:AB_2057371
Mouse anti CNPase	Abcam	Cat #: Ab6319; RRID:AB_2082593
Rabbit anti MBP	Klaus-Armin Nave (Meschkat et al.)[58]	–
Rat anti MBP	Merck	Cat #: MAB386; RRID:AB_94975
Mouse anti MBP	Biolegend	Cat #: 836504; RRID:AB_2616694
Rabbit Ki67	Abcam	Cat #: Ab15580; RRID:AB_443209
Rat anti BrdU	Abcam	Cat #: Ab6326; RRID:AB_305426
Rabbit anti Iba1	Synaptic Systems	Cat #: 234013; RRID:AB_2661873
Mouse anti NeuN	Abcam	Cat #: MAB377; RRID: AB_2298772
Rabbit anti GFAP	Abcam	Cat #: Ab7260; RRID:AB_305808
Rabbit anti CRH	Paul E. Sawchenko	–
Chicken anti GFP	Aves	Cat #: GFP-1020; RRID:AB_10000240
Rabbit anti RFP	Rockland	Cat #: 600-401-379, *RRID*:AB_2209751
Goat anti Rabbit Alexa 488	Invitrogen	Cat #: A-11008
Goat anti Rabbit Alexa 568	Invitrogen	Cat #: A-11011
Goat anti Rabbit Alexa 594	Invitrogen	Cat #: A-11012
Goat anti Rabbit Alexa 647	Invitrogen	Cat #: A-21245
Goat anti Mouse Alexa 488	Invitrogen	Cat #: A-11001
Goat anti Mouse Alexa 568	Invitrogen	Cat #: A-11004
Goat anti Mouse Alexa 594	Invitrogen	Cat #: A-11032
Goat anti Mouse Alexa 647	Invitrogen	Cat #: A-21235
Goat anti Rat Alexa 488	Invitrogen	Cat #: A-11006
Goat anti Rat Alexa 568	Invitrogen	Cat #: A-11077
Goat anti Chicken Alexa 488	Invitrogen	Cat #: A-11039
Goat anti Mouse STAR RED	Abberior	STRED-1001-500UG
Goat anti Rabbit STAR ORANGE	Abberior	STORANGE-1002-500UG
Bacterial and virus strains		
AAV1/2-CMV-DIO-eGFP	Vector Biolabs	VB1396
ssAAV-5/2-hGFAP-hHBbI/E-dlox-dTomato-EGFP(rev)-dlox-WPRE-bGHp(A)	Viral Vector Facility ETH Zurich	v421
Chemicals, peptides, and recombinant proteins		
Green Retrobeads™ IX	Lumafluor	78G180
Experimental models: Organisms/strains		
Mouse: *CRH-Cre* (*Crh*$^{tm1(cre)Zjh}$)	Z. Josh Huang lab Taniguchi et al.[59]	JAX: 012704 MGI:4452089
Mouse: *CRH-FlpO* (*Crh*$^{tm1.1(flpo)Bsab}$)	Bernado Sabatini lab Salimando et al.[60]	JAX: 031559 MGI:6116854
Mouse: *CRHR1-Cre* (*Crhr1*$^{tm4.1(cre)Jde}$)	Dedic et al.[61]	MGI:6201420
Mouse: *CRH-Venus* (*Crh*$^{tm1.1Ksak}$)	Kono et al.[21]	RIKEN: RBRC09893 MGI:6144041

(*Continued on next page*)

Continued

REAGENT or RESOURCE	SOURCE	IDENTIFIER
Mouse: *Tau-LSL-FlpO*	Silvia Arber lab Pivetta et al.[62]	N/A
Mouse: *NG2-CreERT2 (Tg(Cspg4-cre/Esr1*)BAkik)*	Jackson Laboratory, Zhu et al.[63]	JAX: 008538 MGI:4819178
Mouse: *Ai9 (Gt(ROSA)26Sor$^{tm9(CAG-tdTomato)Hze}$)*	Jackson Laboratory, Madisen et al.[64]	JAX: 007909 MGI:3809523
Mouse: *Sun1-GFP (Gt(ROSA)26Sor$^{tm5(CAG-Sun1/sfGFP)Nat}$)*	Mo et al.[65]	JAX: 021039 MGI:5443817
Mouse: *Ai65 (Gt(ROSA)$^{26Sortm65.1(CAG-tdTomato)Hze/J}$)*	Jackson Laboratory Madisen et al.[66]	JAX: 032864 MGI:5478743
Mouse: *Ai65F (Gt(ROSA)$^{26Sortm65.2(CAG-tdTomato)Hze/J}$)*	Jackson Laboratory Madisen et al.[66]	JAX: 032864 MGI:6260212
Mouse: *CRH^{loxP} (Crh$^{tm1.1Jde}$)*	Dedic et al.[61]	MGI:6201415
Mouse: *CRHR1^{loxP} (Crhr1$^{tm2.2Jde}$)*	Kuhne et al.[67]	MGI:5440013
Mouse: *CRHR1$^{\Delta EGFP}$ (Crhr1^{tm1Jde})*	Refojo et al.[24]	MGI:5294436
Software and algorithms		
ImageJ/Fiji	https://imagej.net/downloads	Version 2.0.0-rc-69/1.52

EXPERIMENTAL MODEL AND STUDY PARTICIPANT DETAILS

All animal experiments and protocols were legally approved by the Ethics Committee for the Care and Use of Laboratory Animals of the Government of Upper Bavaria, Germany. 2–6 month old mice were group housed under standard lab conditions (22 ± 1°C, 55 ± 5% humidity) with *ad libitum* access to food and water on a 12:12 h light:dark schedule with weekly cage changes. Regular genotyping was performed by polymerase chain reaction (PCR) analysis of genomic DNA. Global and conditional knockouts were assigned to experimental groups based on their genotype. Age matched littermates were used as controls in all experiments. Mice with incorrect injury or injection were excluded from the experiment. The following mouse lines were used:

CRH-Cre (Crh$^{tm1(cre)Zjh}$),[59] *CRH-FlpO (Crh$^{tm1.1(flpo)Bsab}$)*,[60] *CRHR1-Cre (Crhr1$^{tm4.1(cre)Jde}$)*,[61] *CRH-Venus (Crh$^{tm1.1Ksak}$)*,[21] *Tau-LSL-FlpO,*[62] *NG2-CreERT2 (Tg(Cspg4-cre/Esr1*)BAkik)*,[63] *Ai9 (Gt(ROSA)26Sor$^{tm9(CAG-tdTomato)Hze}$)*,[64] *Sun1-GFP (Gt(ROSA)26Sor$^{tm5(CAG-Sun1/sfGFP)Nat}$)*,[65] *Ai65 (Gt(ROSA)26Sor$^{tm65.1(CAG-tdTomato)Hze}$)*,[66] *Ai65F (Gt(ROSA)$^{26Sortm65.2(CAG-tdTomato)Hze/J}$)*[66], *CRH^{loxP} (Crh$^{tm1.1Jde}$)*,[61] *CRHR1^{loxP} (Crhr1$^{tm2.2Jde}$)*,[67] *CRHR1$^{\Delta EGFP}$ (Crhr1^{tm1Jde})*.[24]

The following double and triple transgenic lines were generated in this study by cross-breeding of single transgenic lines (a detailed description of the lines and their properties can be found in Table S1): *CRH-Cre::Ai9*, *NG2-CreERT2::Ai9*, *CRH-FlpO::NG2-CreERT2::Ai65*, *CRH-FlpO::CRHR1-Cre::Ai65*, *CRH$^{NG2\text{-}cKO}$ (CRH^{loxP}::NG2-CreERT2:: Ai9)*, *CRHR1-Cre:Tau-LSL-FlpO::Ai9*, *CRHR1-Cre::Sun1-GFP*, *CRH-FlpO::Ai65F::CRHR1-Cre::Sun1-GFP.*

METHOD DETAILS

Stereotaxic surgeries

For all experiments requiring stereotaxic surgeries, mice received analgesic treatment prior, during and after surgery. Animals were anesthetized using isoflurane (CP-Pharma) and placed in a stereotaxic frame. Acute injury, fluorescent bead and virus injections, cranial window or hippocampal cannula implantation was performed as described in the sections below.

Acute injury for CRH^{+} OLC quantification and modulation experiments

After opening of the skin and removal of a bone flap using a dental drill, the syringe was slowly inserted and removed from the tissue. The following coordinates were used: PFC: AP 2.2, ML 1.0, DV -3.2; Striatum: AP 1.2, ML 1.5, DV -3.3; MB: AP -3, ML 1.0, DV -4. Injuries were inflicted using a 24-gauge Hamilton syringe. Injuries for label retaining experiments were performed using a 33-gauge Hamilton syringe to reduce background for BrdU staining.

Injection of fluorescent bead and viruses

For injections, head skin was opened. A bone hole was drilled using a dental drill. The syringe was inserted. Then, fluorescent beads (Green Retrobeads IX, Lumafluor, 500 nL), hGFAP-virus (ssAAV-5/2-hGFAP-hHBbI/E-dlox-dTomato-EGFP(rev)-dlox-WPRE-bGHp (A); Viral Vector Facility ETH Zurich, v421, 500 nL) or CMV-eGFP-virus (AAV1/2-CMV-DIO-eGFP, Vector Biolabs, 500 nL) were

injected at a speed of 100 nL/min with a 33 gauge syringe (Hamilton). After injection was finished, the syringe was pulled out 1 mm and, after a waiting time of 2 min, slowly and finally removed from the tissue. The following coordinates were used: AP -3, ML 1.0, DV -3.7.

Cranial window implantation with injury infliction

After stereotaxic fixation, a round piece of skin, ~8 mm in diameter, was removed. Under repeated application of cold saline to prevent overheating, a round piece of cranial bone was drilled out (approx. 5 mm diameter). A double-edged knife was moved in (DV: −0.8 mm) and out of the brain parenchyma three times. A drop of sterile saline was applied to the open brain tissue and a 5 mm coverslip was placed over the opening and subsequently fixed using quick adhesive cement (Parkell C&B Metabond clear powder L, Quick Base B, Universal Catalyst C). The custom-made head plate was positioned on top of the head and fixed using Kallocryl (Speiko, liquid component 1609 and powder 1615).

Implantation of subcortical imaging cannula

Preparation and implantation of the subcortical imaging cannula were performed as described before.[68] The cannula consisted of a cylindrical metal tube, 1.6 mm height and 3.5 mm diameter, sealed at the bottom with a glass coverslip. After stereotaxic fixation of the animals, the head skin was removed. Under repeated application of cold saline to prevent overheating, a round piece of cranial bone (approx. 3.5 mm diameter) was gently carved using a trephine. After removal of the bone flap, the cortex was slowly aspirated using a vacuum pump until the corpus callosum, identified as white matter horizontal fibers, was exposed. The imaging cannula was gently inserted into the cavity and immediately fixed using a quick adhesive cement (Parkell C&B Metabond, clear powder L, Quick base B, Universal Catalyst C). Finally, a custom-made head plate was fixed as described above.

In-vivo 2-photon imaging

2-photon imaging experiments were done using an Ultima IV microscope (Bruker), equipped with an InSight DS + Dual laser system. We used 1040 nm to excite tdTomato, while we tuned the laser to 920 nm wavelength to image the dura. During imaging, the average power at the tissue did not exceed 40 mW. Animals were anesthetized using isoflurane and fixed under the microscope using a custom-made head plate holder. We kept the animals' temperature constant by means of a heating pad set to 37°C. Z-stacks were acquired with 2–5 μm step size using an Olympus XLPlan *N* 25×/1.00 SVMP objective at magnification zoom 1x and 2.38×. We acquired images averaged over 4–16 repetitions per each imaging plane. For time-lapse imaging, images were acquired every 60 s for 20–30 min.

Magnetic resonance imaging (MRI)

MRI experiments were run on a BioSpec 94/20 animal MRI system (Bruker BioSpin GmbH) equipped with a 9.4 T horizontal magnet of 20 cm bore diameter and a BGA12S HP gradient system capable of a maximum gradient strength of 420 mT/m with a 140 μs rise time. Each mouse in the cohort was sedated in a preparation box using 2.5 vol % isoflurane. The animal was then fixed in prone position on an MR compatible animal bed using a stereotactic device, while anesthesia was delivered via a breathing mask. Mice were kept anesthetized with an isoflurane/air mixture (1.5–1.8 vol %, with an air flow of 1.2–1.4 L/min). Respiration and body temperature were constantly monitored using a pressure sensor placed below the mouse's chest and a rectal thermometer, respectively. Body temperature was kept between 36.5°C and 37.5°C using a heating pad. A linear volume resonator coil for excitation of the ^{1}H nuclear spins in combination with a 2 × 2 elements surface array radio frequency coil for reception of their signal were used. After positioning of a mouse in the magnet isocenter, a field map-based shimming was performed to optimize B_0 field homogeneity over the entire mouse brain. Structural T2–weighted (T2w) images were acquired using a 2D multi-slice RARE sequence (RARE factor = 8, TE_{eff}/TR = 33/2500 ms).

Magnetization transfer (MT) to assess molecular proton fraction (MPF)

Magnetization transfer (MT) methods in MRI can be used to estimate the Macromolecular Proton Fraction (MPF) which has been shown to be a sensitive biomarker of myelin density.[27–31] The protocol was derived from recommendations given in Soustelle et al.[30]; Hertanu et al.[31] First, four averages of an MT prepared spoiled gradient recall experiment (MT-SPGR) were acquired, using a preparation Gaussian saturation rf-pulse of 10.25 ms at an offset frequency of 6 kHz and a flip angle of 600°, resulting in a B_{1peak} of 9.1μT.[30] This pulse was followed by an SPGR with an echo time TE of 2.2 ms and a recovery time TR of 30 ms. The matrix size for the experiment was 128 × 128 × 64, with a field of view of 15 × 15 × 25 mm^3, resulting in a resolution of 0.1 × 0.1 × 0.39 mm^3. The duration of the experiment was 14 min and 20 s. Second, variable flip angle (VFA-) SPGR sequences were performed for T1 (R1) quantification. Three such sequences were recorded using flip angles of respectively 6°, 10° and 25°. TE, TR, matrix size, field of view, resolution and number of averages for each of the three VFA-SPGRs were the same as for the MT-SPGR, resulting in the same duration for each of them. Third and last, a B_1^+ mapping experiment was recorded with the actual flip angle imaging (AFI) method.[69] TE was 2.388 ms, TR 15 ms and the flip angle was 60°. The matrix size was 44 × 44 × 40, the field of view 15 × 15 × 25 mm^3 resulting in a resolution of 0.341 × 0.341 × 0.625 mm^3. With a number of averages of four, the duration for the experiment was 6 min 37 s.

Based on these (MT-, T1 and B_1^+) experiments plus the B_0 map obtained from the field map recorded in order to perform the map-based shimming, our data could be prepared to use the software freely available at https://github.com/lsoustelle/qMT in order to derive the MPF for each individual animal.[31,70,71] From these individual maps, an MPF template could be derived using routines in the Advanced Normalization Tools (ANTs) software (http://stnava.github.io/ANTs/). First a few representatives, manually aligned, individual MPF maps were co-registered and merged together into a starting template. Then the routine antsMultivariateTemplateConstruction2.sh in the ANTs software was used to build a template based on all the MPF maps corresponding to each animal in the cohort. Each individual map could then be, in turn, normalized to the newly created template.

Experimental setup for modulation of CRH/CRHR1 system in glial cells

For experiments with inducible Cre recombinase lines, recombination was induced by i.p. injection of TAM two times within the 7 days before injury infliction. For modulation experiments, animals were injured or injected as described above. Mice were sacrificed at 3 or 7 dpi and analyzed for number of OLs ($CC1^+/Olig2^+$), OPCs ($CC1^-/Olig2^+$), all OLCs ($Olig2^+$) and the percentage of OLs of all OLCs ($CC1^+$ of all $Olig2^+$ cells).

Quantification of $CD31^+$ vascularization

For preprocessing of images custom Fiji macros complemented with segmentation by the machine learning assisted image analysis tool Ilastik was used. In brief, the preprocessed and z-projected image was segmented using Ilastik. The segmented binary picture was skeletonized and analyzed using Fijis built-in Skeletonize (2D/3D) and Analyze-Skeleton (2D/3D) functions. Total length of vasculature was analyzed from the extracted data (Methods S2).

Label retaining experiment

BrdU 1 mg/kg was added to the drinking water (1% w/w sucrose). In case of injury experiments, treatment started at the day of injury infliction and was sustained for a maximum of 7 days (7 dpi and 6 wpi mice) or until sacrifice (3 dpi). For naive labeling of CRHR1 KO mice, treatment was applied for two consecutive weeks followed by a retaining time of three weeks.

Cryosectioning

Animals were sacrificed by an overdose of isoflurane and subsequently perfused with ice-cold 1× PBS and 4% PFA. After recovery of the brain, it was post fixed in 4% PFA on ice for 6 h, transferred to 30% sucrose in 1xPBS and incubated at 4°C for 48 h. Brains were frozen on dry ice and cut either coronally or horizontally in 40 μm sections using a cryostat (Leica). Sections were collected in cryoprotection solution (25% Ethylene glycol, 25% glycerol, 50% ddH2O in 1xPBS) and stored at −20°C until further use. For DISH mice were killed by cervical dislocation. After fast recovery the brain was frozen on dry ice and stored at −80°C until further use. Coronal sections (20 μm) were generated using a cryostat (Leica). After thaw-mounting onto SuperFrost slides, sections were dried and kept at −80°C.

Immunofluorescence staining

Immuno fluorescence staining was conducted using different protocols depending on the combination of antigens of interest. For NG2/Olig2 and NG2/Ki67 staining, a two-day protocol was performed. In brief, slices were washed 3x in 1× PBS, followed by blocking in 2% normal goat serum in 0.05% Triton X-100 and 1× PBS. Sections were incubated in primary anti-NG2 antibody at 4°C under shaking overnight. After washing, sections were incubated in secondary antibodies for 2 h at room temperature (RT). After washing, antigen retrieval (AR) was performed in citrate buffer (75°C, 1 h). After washing, primary anti-Olig2 or anti-Ki67 antibody was incubated as described before. After washing, secondary antibody was applied as described before and sections were washed and mounted using Fluoromount-G mounting medium (+/− DAPI, Invitrogen, 15586276).

For CC1/Olig2, Ki67/Olig2 and Ki67/Olig2/GFP staining, washing was performed followed by AR as described before. After washing, sections were blocked. Primary and secondary antibody incubation were also conducted as described before.

For anti-GFP, anti-GFAP, anti-Vimentin, anti-S100β, anti-IBA1, anti-NeuN, anti-MBP, anti-CNPase and anti-CD31 staining, sections were washed and blocked as described above. Primary and secondary antibody treatment were performed as mentioned above.

For CRH, staining sections were washed and blocked as described before. Primary antibody was added and sections were incubated for 5 days under shaking at 4°C. Secondary antibody treatment was performed as described above.

For BrdU staining, two different protocols were used. Sections were washed and AR was achieved either with citrate buffer (2.94 g/L, pH 6, 1 h, 75°C) for injury sites or with HCl (2 M, 10 min, 37°C) followed by borate buffer (10 min, RT) for naive brains. After washing sections were blocked and primary and secondary antibody staining was performed as described above.

The following primary antibodies and dilutions were used: rb NG2 (1:200, Merck, AB5320), rb Olig2 (1:200, Merck, AB9610), mouse (ms) Olig2 (1:200, Merck, MABN50), ms APC (CC1) (1:200, Merck, OP80), ms CNPase (1:1000, Abcam, ab6319), rb MBP (1:500, obtained from Klaus-Armin Nave, MPI exp. Medicine, Goettingen),[58] rat MBP (1:500, Merck, MAB386), ms MBP (1:200, Biolegend, 836504), rb Ki67 (1:500 - 1:1000, Abcam, Ab15580), rat BrdU (1:500–1:1000, Abcam, 6326), rb Iba1 (1:500–1:1000, Synaptic Systems, 234013), ms NeuN (1:500, Merck, MAB377), rb GFAP (1:500–1:3000, Abcam, ab7260), rb CRH (1:20000, obtained from Paul E. Sawchenko, Salk Institute, La Jolla), chicken (ck) GFP (1:500–1:1000, Aves, GFP-1020), rb RFP (1:500, Rockland,

600-401-379). The following secondary antibodies were used: goat anti rb Alexa 488, Alexa 568, Alexa 594 or Alexa 647, goat anti ms Alexa 488, Alexa 568, Alexa 594 or Alexa 647, goat anti rat Alexa 488 or Alexa 568 and goat anti ck Alexa 488.

For expansion staining following expansion microscopy the following secondary antibodies were used: anti ms STAR RED, Abberior, anti rb STAR ORANGE, Abberior.

Expansion microscopy

Brain sections of *CRHR1-Cre::LSL-FlpO::Ai9* mice were retrieved from cryoprotectant solution and washed three times with 1× PBS. To expand the samples, an adjusted TREx protocol was applied, as previously described.[23,72] Briefly, brain slices were mounted onto super-frost microscope slides and treated with 10 μg/mL acryloyl X-SE in 1× PBS overnight at RT. The gelation solution contained 1.1 M sodium acrylate, 2.0 M acrylamide, 50 ppm N,N′-methylenebisacrylamide and 1× PBS. The polymerization was initiated by the addition of TEMED (1.5 ppt) and APS (1.5 ppt). The process was slowed by 4-Hydroxy-TEMPO (15 ppm) and working on ice to allow for an extended incubation time of 30 min in activated gelation solution, before mounting the slide containing the brain sections into a custom-build gelation chamber plate. The samples were incubated for 2 h at 40°C to allow for full polymerization. Then, slices were recovered into digestion buffer (50 mM Tris-BASE, 200 mM NaCl, 200 mM SDS in ddH_2O, pH 9.0) and incubated for 4 h at 80°C in a Thermo-Block. After denaturation, the samples were rinsed once in ddH_2O and washed several times in 1x PBS to remove residual SDS. At this stage, the region of interest was cut from the gel with a razor blade. For immune fluorescent staining, the samples were incubated for 3 h in blocking solution (0.3% Triton X-100, 3% BSA in 1x PBS), followed by 72 h of incubation with primary antibodies (ms MBP, rb RFP) diluted in blocking solution at 4°C under shaking. Subsequently, secondary antibody incubation (ms STAR RED, rb STAR ORANGE) was performed overnight at 4°C under shaking. The stained gels were then incubated with BODIPY-FL NHS (20 μM, ThermoFisher) in 1× PBS for 1h at RT on a shaker. Afterward, the samples were washed five times in ddH_2O and stored at 4°C overnight to complete the expansion of the gel. For imaging, the gels were placed onto the PLL-coated surface of a #1.5H one-chambered cover glass (Cellvis), sample-side facing down. The samples were then immobilized by embedding them into two-component silicone (eco-sil, picodent), preventing drift and dehydration during imaging.

Image acquisition

Images for quantification of cell numbers and intensity measurements were acquired using an Olympus VS120 Slide Scanner. For overview and close up acquisition, the 4× or 20× objective was used, respectively. Exposure times were chosen to yield the best signal to noise ratio and minimal photodamage. Images were extracted and saved as .tif files.

Qualitative images of cells of interest were taken with a Laser scanning confocal microscope (Carl Zeiss). 20× water-, 40× and 63× oil-immersion objectives were used. Laser settings were adjusted to yield the best signal to noise ratio. Images were acquired with 1024 × 1024 pixel size and a scan speed between 3 and 7.

Quantification of CRH-expressing OPCs in *CRH-Cre::Ai9* mice

A 28 μm z stack with a step size of 3 μm was acquired around the injury site. The counting matrix was generated with a custom Fiji macro. Cells in the different areas between ±300 μm were counted using Fiji's manual counting tool. To generate comparable counts, consistent contrast settings were used for each quantification.

Quantification of CRHR1-expressing OLCs at 1.5, 3 and 5 months in *CRHR1-Cre::LSL-FlpO::Ai9* mice

After CC1/Olig2 or NG2/Olig2 staining was performed, z-stacks (28 μm depth, 3 μm step size, 1 mm^2 ROI) were acquired in CX, CC, AC, OT and MB. CC1 and NG2/tdTomato co-expressing cells were quantified in the whole ROI. The number of all $Olig2^+$ cells was counted in a consistent subregion (64000 μm^2) and upscaled to cells/mm^2.

Quantification of cells in CRH/CRHR1 system modulation experiments

Horizontal sections were imaged as described above. After setting the wound center, the circular counting matrix with a radius of 300 μm and medio-lateral resolution of 50 μm was generated using a custom macro in Fiji (Methods S1). In the increased injury size experiment coronal sections were analyzed to increase the visible section of the injury. These injuries were analyzed using the rectangular counting matrix with a medio-lateral resolution of 50 μm which was semi-automatically created using a custom Fiji macro. Because of variations in the visible part of the wound and, hence, the height of the analyzed ROI the numbers are presented as cells/mm^2. Cells were counted with the manual Fiji counting tool. Consistent contrast settings were used for each quantification.

MRI analysis

MPF images were analyzed in SPM12 (www.fil.ion.ucl.ac.uk/spm/software/spm12/) using a full factorial model with factors sex (male and female) and genotype (WT and KO). For each of the four groups, $n = 8$ animals were included in the final analysis. The whole brain analysis, excluding the CSF space using an implicit intensity mask, was run without global normalization, as the MPF is an absolute measure. F-contrasts of the main effects of sex or genotype were calculated, along with the interaction sex × genotype. To detect statistical differences, a post-hoc t test showing the negative effect of genotype with a $p_{FDR,\ cluster} < 0.05$, at a collection threshold of $p < 0.01$ was conducted.

Electron microscopy

Samples were prepared according to Weil and colleagues.[73] In brief, animals were sacrificed using isoflurane and perfused with 1× PBS (pH 7.4) and subsequently with fixative solution (4% PFA, 2.5% glutaraldehyde in phosphate buffer with 0.5% NaCl, pH 7.4). Brains were dissected and postfixed in same fixative overnight at 4°C. For targeting the region of interest, sagittal vibratome slices were prepared with a Leica VT1200S (Leica, Wetzlar, Germany) and pieces of medial and lateral rostral corpus callosum were extracted from the vibratome slices using a biopsy punch. These pieces were postfixed with 2% OsO4 (Science Services, München, Germany) in 0.1 M phosphate buffer pH 7.3 and embedded in EPON resin (Serva, Heidelberg, Germany) after dehydration with acetone. Ultrathin sections were prepared using a Leica UC7 ultramicrotome (Leica, Wetzlar, Germany) and a 35° diamond knife (Diatome, Biel, Switzerland) and stained with UranylLess (Science Services, Munich, Germany). EM pictures were taken with a Zeiss EM912 electron microscope (Carl Zeiss Microscopy GmbH, Oberkochen, Germany) using an on-axis 2k CCD camera (TRS, Moorenweis, Germany).

G ratio measurement and analysis

Image analysis was performed with ImageJ (Fiji, Version 2.0.0-rc-69/1.52). For g ratio analysis, 12 random overview EM pictures (at 5000× magnification) corpus callosum sections were taken and 300–350 axons per animal were analyzed. For g ratio analysis (axon diameter divided by the axon diameter including the myelin sheath) diameters were determined from circular areas equivalent to the measured areas. The analysis was carried out blinded with regard to the genotype.

QUANTIFICATION AND STATISTICAL ANALYSIS

For statistical analysis, GraphPad Prism 8 was used. One-way ANOVA followed by Bonferroni's and two-way ANOVA followed by Sidak's post hoc test were performed. Students T test or Whitney U test were performed. The used test is indicated in the figure legend. Values are reported as means ± standard error of mean (SEM). Statistical significance was defined as $p < 0.05$. p values are shown as asterisk ($^{*}p < 0.05$, $^{****}p < 0.0001$). Number of animals is reported in the figure legends and indicated as n_{TP} (animals per timepoint), n_{GT} (animals per genotype), nTP/GT (animals per timepoint and genotype) and n (total number of animals). No statistical methods were used to predetermine sample sizes, but it was based on those previously reported in other publications.[4,14] During analysis, experimenters were blinded to experimental conditions.